Mon. Not. R. Astron. Soc. **000**, 1–14 (2002)

Atmospheres and Spectra of Strongly Magnetized Neutron Stars II: Effect of Vacuum Polarization

Wynn C. G. Ho and Dong Lai
Center for Radiophysics and Space Research, Department of Astronomy, Cornell University Ithaca, NY 14853, USA
E-mail: wynnho@astro.cornell.edu, dong@astro.cornell.edu

Accepted 2002 xxx, Received 2002 xxx; in original form 2002 xxx

ABSTRACT

We study the effect of vacuum polarization on the atmosphere structure and radiation spectra of neutron stars with surface magnetic fields $B = 10^{14} - 10^{15}$ G, as appropriate for magnetars. Vacuum polarization modifies the dielectric property of the medium and gives rise to a resonance feature in the opacity; this feature is narrow and occurs at a photon energy that depends on the plasma density. Vacuum polarization can also induce resonant conversion of photon modes via a mechanism analogous to the MSW mechanism for neutrino oscillation. We construct atmosphere models in radiative equilibrium with an effective temperature of a few $\times 10^6$ K by solving the full radiative transport equations for both polarization modes in a fully ionized hydrogen plasma. We discuss the subtleties in treating the vacuum polarization effects in the atmosphere models and present approximate solutions to the radiative transfer problem which bracket the true answer. We show from both analytic considerations and numerical calculations that vacuum polarization produces a broad depression in the X-ray flux at high energies (a few keVEa few tens of keV) as compared to models without vacuum polarization; this arises from the density dependence of the vacuum resonance feature and the large density gradient present in the atmosphere. Thus the vacuum polarization effect softens the high energy tail of the thermal spectrum, although the atmospheric emission is still harder than the blackbody spectrum because of the non-grey opacities. We also show that the depression of continuum flux strongly suppresses the equivalent width of the ion cyclotron line; this may help to explain the absence of line features in recent *Chandra* and *XMM-Newton* observations of several magnetar candidates.

Key words: magnetic fields – radiative transfer – stars: atmospheres – stars: magnetic fields – stars: neutron – X-rays: stars

1 INTRODUCTION

Thermal radiation from the surface of isolated neutron stars (NSs) can provide invaluable information on the physical properties and evolution of NSs. In the last few years, such radiation has been detected in four types of isolated NSs: (1) radio pulsars (see Becker 2000), (2) old, radio-quiet NSs (not associated with supernova remnants), some of which may be accreting from the interstellar medium (see Treves et al. 2000), (3) soft gamma-ray repeaters (SGRs) and anomalous X-ray pulsars (AXPs) (see Mereghetti 1999; Hurley 2000; Israel, Mereghetti, & Stella 2001; Perna et al. 2001), which form a potentially new class of NSs ("magnetars") endowed with superstrong ($B10^{14}$ G) magnetic fields (see Thompson & Duncan 1996; Thompson 2000), and (4) young, radio-quiet NSs in supernova remnants, which may include AXPs or SGRs (see Pavlov et al. 2001). The NS surface emission is mediated by the thin atmospheric layer (with scale height $\sim 0.1 - 10$ cm and density $\sim 0.1 - 100$ g/cm^3) that covers the stellar surface. Therefore, to properly interpret the observations of NS surface emission and to provide accurate constraints on the physical properties of NSs, it is important to understand in detail the radiative properties of NS atmospheres in the presence of strong magnetic fields (see Pavlov et al. 1995 and Ho & Lai 2001 for more detailed references on observations and on previous works of NS atmosphere modeling).

This paper is the second in a series where we systematically investigate the atmosphere and spectra of strongly magnetized NSs. In Ho & Lai (2001, hereafter Paper I), we constructed self-consistent NS atmosphere models in radiative equilibrium with magnetic field $B \sim 10^{12} - 10^{15}$ G and $T_{\rm eff} \sim 10^6 - 10^7$ K and assuming the atmosphere is composed of fully ionized hydrogen or helium. The radiative opacities include free-free absorption and scattering by both electrons and ions computed for the two photon po-

larization modes in the magnetized electron-ion plasma. It was found that, in general, the emergent thermal radiation exhibits significant deviation from blackbody, with harder spectra at high energies; the spectra can also show a broad feature ($\Delta E/E_{Bi} \sim 1$) around the ion cyclotron resonance $E_{Bi} = 0.63\,(Z/A)(B/10^{14}\ \mathrm{G})$ keV, where Z and A are the atomic charge and atomic mass of the ion, respectively (see also Zane et al. 2001), and this feature is particularly pronounced when $E_{Bi} 3kT_{\rm eff}$ (however, as we show in this paper, vacuum polarization can significantly diminish the equivalent width of the ion cyclotron feature; see Sections 4 and 6).

In this paper, we study the effect of vacuum polarization on the atmosphere structure and radiation spectra of strongly magnetized NSs. It is well-known that polarization of the vacuum due to virtual e^+e^- pairs becomes significant when $BB_{\rm Q}$, where $B_{\rm Q} = m_e^2c^3/e\hbar = 4.414 \times 10^{13}$ G is the magnetic field at which the electron cyclotron energy $\hbar\omega_{Be} = \hbar eB/m_ec$ equals m_ec^2. Vacuum polarization modifies the dielectric property of the medium and the polarization of photon modes (e.g., Adler 1971; Tsai & Erber 1975; Gnedin, Pavlov, & Shibanov 1978; Heyl & Hernquist 1997b), thereby altering the radiative scattering and absorption opacities (e.g., Mészáros & Ventura 1979; Pavlov & Gnedin 1984; see Mészáros 1992 for review). Of particular interest is the "vacuum resonance" phenomenon, which occurs when the effects of the vacuum and plasma on the linear polarization of the modes cancel each other, giving rise to "resonant" features in the radiative opacities (e.g., Pavlov & Shibanov 1979; Ventura, Nagel, & Mészáros 1979; Bulik & Miller 1997). At a given density ρ, the vacuum-induced resonance is located at the photon energy

$$E_{\rm V} \approx 1.02 \left(\frac{Y_e\rho}{1\ \mathrm{g\ cm^{-3}}}\right)^{1/2} \left(\frac{B}{10^{14}\ \mathrm{G}}\right)^{-1} f(B)\ \mathrm{keV}, \qquad (1.1)$$

where $Y_e = Z/A$ is the electron fraction and $f(B)$ is a slowly-varying function of B [$f(B) = 1$ for $B \ll B_{\rm Q}$ and is of order a few for $B \sim 10^{14} - 10^{16}$ G; see Section 2]. It has been suggested that this vacuum resonance may manifest itself as absorption-like features in the spectra of X-ray pulsars and magnetars (e.g., Ventura, Nagel, & Mészáros 1979; Bulik & Miller 1997). However, as we show both analytically and numerically in this paper, since the atmosphere spans a wide range of densities and $E_{\rm V}$ depends on ρ, the spectral feature associated with $E_{\rm V}$ is spread out significantly and manifests as a broad "depression" in the radiation spectrum.

Furthermore, in a recent paper (Lai & Ho 2001, hereafter Paper II), we showed that there is a new physical effect associated with the vacuum resonance: a photon propagating outward in the NS atmosphere can convert from one polarization mode into another as it traverses the resonant density $\rho_{\rm V}$, which is given by

$$\rho_{\rm V} \approx 0.96\, Y_e^{-1} \left(\frac{E}{1\ \mathrm{keV}}\right)^2 \left(\frac{B}{10^{14}\ \mathrm{G}}\right)^2 f(B)^{-2}\ \mathrm{g\ cm^{-3}}. \quad (1.2)$$

This resonant mode conversion is analogous to the Mikheyev-Smirnov-Wolfenstein (MSW) effect for neutrino oscillations (e.g., Bahcall 1989; Haxton 1995) and is effective for E a few keV (for which the propagation is adiabatic) and ineffective for E a few keV (the adiabatic condition breaks down). Because the two photon modes have vastly different opacities, this vacuum-induced mode conversion can significantly affect radiative transport in magnetar atmospheres. To properly account for this mode conversion effect in the atmosphere models, one must go beyond the modal description of the radiation field by formulating and solving the transfer equation in terms of the photon density matrix and including the effect of the refractive index. This is beyond the scope of this paper. Instead, we consider two limiting cases in this paper: no mode conversion and complete mode conversion. These two limits correspond to different ways of labeling the photon modes, and the resulting model atmosphere spectra should approximately bracket the true spectra.

There have been few previous works studying the effect of vacuum polarization on the radiation spectra of strongly magnetized NSs. Bezchastnov et al. (1996) reported NS atmosphere models with $B \sim 10^{14} - 10^{16}$ G and $T_{\rm eff} \approx 10^8$ K. This temperature is not appropriate for SGRs and AXPs, which have $T_{\rm eff} \sim$ a few $\times 10^6$ K (see, e.g., Mereghetti 1999; Perna et al. 2001). Although the vacuum-induced mode conversion was not discussed, the labeling of the photon modes in Bezchastnov et al. (1996) amounts to assuming complete mode conversion (see Section 2.4). Bulik & Miller (1997) considered how blackbody radiation with $T \approx 10^8$ K is modified as it passes through a tenuous plasma where the opacity is affected by vacuum polarization, but no self-consistent atmosphere modeling, which is needed to determine the density and temperature profiles, was attempted, and mode conversion was neglected. Özel (2001) studied magnetar atmosphere models (with $B10^{14}$ G and $T_{\rm eff} \sim$ a few $\times 10^6$ K) which include the effect of vacuum polarization on the opacities (see also Shibanov et al. 1992 for $B \sim 10^{12}$ G atmosphere models which include a similar vacuum polarization effect on the opacities). Besides neglecting resonant mode conversion, Özel's work also neglects the ion effect and adopts a "saturation" scheme to smooth out the vacuum resonance feature in the opacity. Our analytical and numerical consideration of the vacuum resonance feature shows that such a "saturation" scheme cannot be justified (see Sections 3 and 6.3). Indeed, as we discuss in this paper, even when neglecting resonant mode conversion, great care must be taken to properly handle the narrow and density-dependent vacuum-induced opacity feature in the radiative transport (see Section 5).

In Section 2, we study the effect of vacuum polarization on the photon propagation modes in a magnetized electron-ion plasma and clarify the nature of the vacuum resonance and the associated mode conversion phenomenon. In Section 3, we discuss the change in the radiative opacities as a result of vacuum polarization. Section 4 shows the qualitative effect of the vacuum resonance feature on the NS surface emission. The difficulties encountered in solving the radiative transfer equation caused by vacuum polarization is discussed in Section 5. We present atmosphere models and spectra for different magnetic field strengths in Section 6. Section 7 summarizes and discusses the implications of our results. Several "toy" atmosphere models that include opacities which mimic the vacuum polarization effects are discussed in Appendix A1.

2 PHOTON POLARIZATION MODES IN A MAGNETIZED ELECTRON-ION PLASMA INCLUDING VACUUM POLARIZATION

In this section, we outline the derivation of the photon polarization modes in a magnetized electron-ion plasma including the effect of vacuum polarization. Previous studies (e.g., Mészáros & Ventura 1979) neglected the ion effect and/or considered the $B \ll B_{\rm Q}$ limit. Following the standard convention, the two normal modes are termed the extraordinary mode (X-mode, $j = 1$), which is mostly polarized perpendicular to the k-B plane, and the ordinary mode (O-mode, $j = 2$), which is mostly polarized parallel to the k-B plane, where k is the wave vector along the wave propagation direction and B is the external magnetic field (e.g., Mészáros 1992). We shall see that this classification of the modes becomes ambiguous near the vacuum resonance, where mode conversion can occur (Sections 2.3 and 2.4).

2.1 Dielectric and Permeability Tensors

For a cold electron-ion plasma, the plasma contribution to the dielectric tensor $^{(\rm p)}$ can be written, in the coordinate system $x'y'z'$ with B along z', as (e.g., Shafranov 1967)

$$\left[{}^{(\rm p)}\right]_{\hat{z}'=\hat{B}} = \left[\begin{array}{ccc} \varepsilon & ig & 0 \\ -ig & \varepsilon & 0 \\ 0 & 0 & \eta \end{array}\right], \tag{2.1}$$

where

$$\varepsilon = 1 - \sum_s \frac{\lambda_s v_s}{\lambda_s^2 - u_s} \approx 1 - v_{\rm e}\frac{1 - M u_{\rm i}}{(1-u_{\rm i})(1-u_{\rm e})} \tag{2.2}$$

$$\eta = 1 - \sum_s \frac{v_s}{\lambda_s} \approx 1 - v_{\rm e} \tag{2.3}$$

$$g = -\sum_s \frac{{\rm sign}(q_s) u_s^{1/2} v_s}{\lambda_s^2 - u_s} \approx \frac{v_{\rm e} u_{\rm e}^{1/2}}{(1-u_{\rm i})(1-u_{\rm e})}. \tag{2.4}$$

In equations (2.2)-(2.4), the sums run over each charged particle species s (electron and ion) in the plasma, and $u_s = \omega_{Bs}^2/\omega^2$ and $v_s = \omega_{\rm ps}^2/\omega^2$, where $\omega_{Bs} = |q_s|B/(m_s c)$ is the cyclotron frequency and $\omega_{\rm ps} = (4\pi n_s q_s^2/m_s)^{1/2}$ is the plasma frequency of charged particle s. Damping of the particle motion is accounted for by $\lambda_s = 1 + i\nu_s/\omega$, where ν_s is the damping rate. In the second equalities of equations (2.2)-(2.4), we have taken the $M \equiv Am_{\rm p}/(Zm_{\rm e}) = v_{\rm e}/v_{\rm i} = (u_{\rm e}/u_{\rm i})^{1/2} \gg 1$ limit and assumed small damping ($\nu_s \ll \omega$ or $\lambda_s \to 1$). The relevant dimensionless parameters are

$$u_{\rm e} = \frac{\omega_{Be}^2}{\omega^2}, \qquad u_{\rm i} = \frac{\omega_{Bi}^2}{\omega^2}, \qquad v_{\rm e} = \frac{\omega_{\rm pe}^2}{\omega^2}, \tag{2.5}$$

where the electron cyclotron frequency ω_{Be}, the ion cyclotron frequency ω_{Bi}, and the electron plasma frequency $\omega_{\rm pe}$ are given by

$$E_{Be} = \hbar\omega_{Be} = \hbar\frac{eB}{m_{\rm e}c} = 1.158\, B_{14}\ {\rm MeV} \tag{2.6}$$

$$E_{Bi} = \hbar\omega_{Bi} = \hbar\frac{ZeB}{Am_{\rm p}c} = 0.6305\, B_{14}\left(\frac{Z}{A}\right)\ {\rm keV} \tag{2.7}$$

$$E_{\rm pe} = \hbar\omega_{\rm pe} = \hbar\left(\frac{4\pi e^2 n_{\rm e}}{m_{\rm e}}\right)^{1/2} = 28.71\left(\frac{Z}{A}\right)^{1/2}\rho_1^{1/2}\ {\rm eV}, \tag{2.8}$$

respectively, $B_{14} = B/(10^{14}\ {\rm G})$, and $\rho_1 = \rho/(1\ {\rm g\ cm^{-3}})$.

Vacuum polarization contributes a correction to the dielectric tensor:

$$\Delta^{(\rm v)} = (a-1)\,\mathbf{I} + q\hat{B}\hat{B}, \tag{2.9}$$

where $\mathbf{I}$ is the unit tensor and $\hat{B} = B/B$ is the unit vector along B. The magnetic permeability tensor also deviates from unity because of vacuum polarization; the magnetic field $H_{\rm w}$ of an electromagnetic wave is related to its magnetic induction $B_{\rm w}$ by

$$H_{\rm w} = {}^{-1}\cdot B_{\rm w} = \left(a\mathbf{I} + m\hat{B}\hat{B}\right)\cdot B_{\rm w}. \tag{2.10}$$

For $\hbar\omega \ll m_{\rm e}c^2$, general expressions for the vacuum polarization coefficients a, q, and m are given in Heyl & Hernquist (1997a). In the weak-field limit, $B \ll B_{\rm Q} = 4.414\times10^{13}$ G, they are given by

$$a = 1 - 2\delta_{\rm V} \tag{2.11}$$

$$q = 7\delta_{\rm V} \tag{2.12}$$

$$m = -4\delta_{\rm V}, \tag{2.13}$$

where

$$\delta_{\rm V} = \frac{\alpha_{\rm F}}{45\pi}b^2, \tag{2.14}$$

$\alpha_{\rm F} = e^2/\hbar c = 1/137$ is the fine structure constant and $b = B/B_{\rm Q}$ (Adler 1971). For $BB_{\rm Q}$, we use the expansions given in Heyl & Hernquist (1997a,b; see also Tsai & Erber 1975) to find

$$a \approx 1 + \frac{\alpha_{\rm F}}{2\pi}\left[1.195 - \frac{2}{3}\ln b - \frac{1}{b}\left(0.8553 + \ln b\right) - \frac{1}{2b^2}\right] \tag{2.15}$$

$$q \approx -\frac{\alpha_{\rm F}}{2\pi}\left[-\frac{2}{3}b + 1.272 - \frac{1}{b}\left(0.3070 + \ln b\right) - 0.7003\frac{1}{b^2}\right] \tag{2.16}$$

$$m \approx -\frac{\alpha_{\rm F}}{2\pi}\left[\frac{2}{3} + \frac{1}{b}\left(0.1447 - \ln b\right) - \frac{1}{b^2}\right]. \tag{2.17}$$

When $|\Delta\epsilon_{ij}^{(\rm v)}| \ll 1$ or $b \ll 3\pi/\alpha_{\rm F}$ ($B \ll 5\times10^{16}$ G), the plasma and vacuum contributions to the dielectric tensor can be added linearly, i.e., $ = {}^{(\rm p)} + \Delta^{(\rm v)}$. In the frame with $\hat{B}$ along $\hat{z}'$,

$$[]_{\hat{z}'=\hat{B}} = \left[\begin{array}{ccc} \varepsilon & ig & 0 \\ -ig & \varepsilon & 0 \\ 0 & 0 & \eta \end{array}\right] + \left[\begin{array}{ccc} \hat{a} & 0 & 0 \\ 0 & \hat{a} & 0 \\ 0 & 0 & \hat{a}+q \end{array}\right] = \left[\begin{array}{ccc} \varepsilon' & ig & 0 \\ -ig & \varepsilon' & 0 \\ 0 & 0 & \eta' \end{array}\right], \tag{2.18}$$

where $\hat{a} = a - 1$, $\varepsilon' = \varepsilon + \hat{a}$, and $\eta' = \eta + \hat{a} + q$. The total magnetic permeability is given by equation (2.10).

2.2 Equations for the Polarization Modes

Using the electric displacement $D = \cdot E$ and equation (2.10) in the Maxwell equations, we obtain the equation for plane waves with $E \propto e^{i(k\cdot r - \omega t)}$:

$$\left\{\frac{1}{a}\epsilon_{ij} + n^2\left[\hat{k}_i\hat{k}_j - \delta_{ij} - \frac{m}{a}(\hat{k}\times\hat{B})_i(\hat{k}\times\hat{B})_j\right]\right\}E_j = 0, \tag{2.19}$$

where $n = ck/\omega$ is the refractive index and $\hat{k} = k/k$. In the coordinate system xyz with k along the z-axis and B in the x-z plane, such that $\hat{k} \times \hat{B} = \sin\theta_B \hat{y}$ (θ_B is the angle between $\hat{k}$ and $\hat{B}$), the dielectric tensor [eq. (2.18)] is given by

$$[]_{\hat{z}=\hat{k}} = \left[\begin{array}{ccc} \varepsilon' \cos^2\theta_B + \eta' \sin^2\theta_B & ig\cos\theta_B & (\varepsilon'-\eta')\sin\theta_B\cos\theta_B \\ -ig\cos\theta_B & \varepsilon' & -ig\sin\theta_B \\ (\varepsilon'-\eta')\sin\theta_B\cos\theta_B & ig\sin\theta_B & \varepsilon'\sin^2\theta_B + \eta'\cos^2\theta_B \end{array} \right]. \quad (2.20)$$

The z-component of equation (2.19) gives

$$E_z = -\epsilon_{zz}^{-1}\left(\epsilon_{zx}E_x + \epsilon_{zy}E_y\right). \quad (2.21)$$

Reinserting this back into equation (2.19) yields

$$\left(\begin{array}{cc} \eta_{xx} - n^2 & \eta_{xy} \\ \eta_{yx} & \eta_{yy} - rn^2 \end{array} \right) \left(\begin{array}{c} E_x \\ E_y \end{array} \right) = 0, \quad (2.22)$$

where $r = 1 + \hat{r} \equiv 1 + (m/a)\sin^2\theta_B$ and

$$\eta_{xx} = \frac{1}{a\epsilon_{zz}}\left(\epsilon_{zz}\epsilon_{xx} - \epsilon_{xz}\epsilon_{zx}\right) = \frac{1}{a\epsilon_{zz}}\varepsilon'\eta' \quad (2.23)$$

$$\eta_{yy} = \frac{1}{a\epsilon_{zz}}\left(\epsilon_{zz}\epsilon_{yy} - \epsilon_{yz}\epsilon_{zy}\right) = \frac{1}{a\epsilon_{zz}}\left[\left(\varepsilon'^2 - g^2 - \varepsilon'\eta'\right)\sin^2\theta_B + \varepsilon'\eta'\right] \quad (2.24)$$

$$\eta_{yx} = -\eta_{xy} = \frac{1}{a\epsilon_{zz}}\left(\epsilon_{zz}\epsilon_{yx} - \epsilon_{yz}\epsilon_{zx}\right) = \frac{1}{a\epsilon_{zz}}\left(-ig\eta'\cos\theta_B\right). \quad (2.25)$$

We write the unit polarization vector as

$$E = e^j = \frac{1}{(1 + K_j^2 + K_{z,j}^2)^{1/2}}(iK_j, 1, iK_{z,j}), \quad (2.26)$$

where $iK_j = E_x/E_y$, $iK_{z,j} = E_z/E_y$, and j is the mode index ($j = 1$ for the X-mode, and $j = 2$ for the O-mode). Eliminating n^2 from equation (2.22), we obtain

$$K_j = \beta\left[1 + (-1)^j\left(1 + \frac{r}{\beta^2}\right)^{1/2}\right]. \quad (2.27)$$

The polarization parameter β is given by

$$\beta = -i\frac{r\eta_{xx} - \eta_{yy}}{2\eta_{yx}} = -\frac{\left(\varepsilon'^2 - g^2 - \varepsilon'\eta'\right)\sin^2\theta_B + \varepsilon'\eta'(1-r)}{2g\eta'\cos\theta_B}. \quad (2.28)$$

Using $\varepsilon' = \varepsilon + \hat{a}$ and $\eta' = \eta + \hat{a} + q$ [see eq. (2.18)] and $1 - r = -(m/a)\sin^2\theta_B$, we write

$$\beta = \beta_0\beta_{\rm V}, \quad (2.29)$$

where β_0 is the polarization parameter in the absence of vacuum polarization

$$\beta_0 = -\frac{\left(\varepsilon^2 - g^2 - \varepsilon\eta\right)\sin^2\theta_B}{2g\eta\cos\theta_B} = \frac{u_{\rm e}^{1/2}}{2(1-v_{\rm e})}\frac{\sin^2\theta_B}{\cos\theta_B}\left(1 - u_{\rm i} - \frac{1+v_{\rm e}}{M}\right) \quad (2.30)$$

and $\beta_{\rm V}$ is the correction factor due to vacuum polarization

$$\beta_{\rm V} = \left(1 + \frac{\hat{a}+q}{\eta}\right)^{-1}\left[1 + \frac{\varepsilon(\hat{a}-q) - \eta\hat{a} - \varepsilon\eta m}{\varepsilon^2 - g^2 - \varepsilon\eta}\right] = \left(1 + \frac{\hat{a}+q}{1-v_{\rm e}}\right)^{-1}\left\{1 + \frac{(q+m)(1-u_{\rm e})}{u_{\rm e}v_{\rm e}} \times \left[\frac{(1-u_{\rm i})\left(1 - \frac{\hat{a}+m}{q+m}v_{\rm e}\right) - \frac{v_{\rm e}(1-Mu_{\rm i})}{1-u_{\rm e}}\frac{-\hat{a}+q+m(1-v_{\rm e})}{q+m}}{1 - u_{\rm i} - M^{-1}(1+v_{\rm e})}\right]\right\}. \quad (2.31)$$

For $v_{\rm e} \ll 1$, equation (2.31) simplifies to

$$\beta_{\rm V} \approx 1 + \frac{(q+m)(1-u_{\rm e})}{u_{\rm e}v_{\rm e}}. \quad (2.32)$$

In addition, from equation (2.21), we find

$$K_{z,j} = -\frac{(\varepsilon - \eta - q)\sin\theta_B\cos\theta_B K_j + g\sin\theta_B}{\varepsilon\sin^2\theta_B + (\eta+q)\cos^2\theta_B + \hat{a}} = \left[u_{\rm e}v_{\rm e}\left(1 - u_{\rm i} - \frac{1}{M}\right)\sin\theta_B\cos\theta_B K_j \times \left(1 + q\frac{1-u_{\rm e}}{u_{\rm e}v_{\rm e}}\frac{1-u_{\rm i}}{1-u_{\rm i}-M^{-1}}\right) - u_{\rm e}^{1/2}v_{\rm e}\sin\theta_B\right] \times \left\{(1-u_{\rm e})(1-u_{\rm i})\left(1 + \hat{a} + q\cos^2\theta_B\right) - v_{\rm e}\left[(1-u_{\rm i})\left(1 - u_{\rm e}\cos^2\theta_B\right) - Mu_{\rm i}\sin^2\theta_B\right]\right\}^{-1}. \quad (2.33)$$

It is evident from equation (2.33) that the component of e^j along k is of order $v_{\rm e} \propto \rho/\omega^2$, and thus, at sufficiently low densities, $K_{z,j}$ can be neglected so that the modes are transverse.

Finally, the refractive index n_j of the mode can be obtained from equation (2.22), which gives

$$n_j^2 = \frac{g\eta'}{a\epsilon_{zz}}\left(\frac{\varepsilon'}{g} + \frac{1}{K_j}\cos\theta_B\right), \quad (2.34)$$

where $\epsilon_{zz} = \varepsilon'\sin^2\theta_B + \eta'\cos^2\theta_B$ [see eq. (2.20)] and ε', η', g, and a are as given in equation (2.18).

2.3 Vacuum Resonance

The polarization parameter β [eqs. (2.28)-(2.32)] directly determines the characteristics of photon normal modes in the medium. For most energies (away from the resonance points, where $\beta = 0$; see below), $|\beta| \propto u_{\rm e}^{1/2} \gg 1$, and we have

$$K_1 \approx -\frac{r}{2\beta} \approx -\frac{1}{2\beta}, \qquad K_2 \approx 2\beta \qquad (|\beta| \gg 1). \quad (2.35)$$

Thus the extraordinary mode ($j = 1$) is almost linearly polarized with its electric field perpendicular to the k-B plane, while the electric field of the ordinary mode ($j = 2$) is in the k-B plane.

The condition $\beta = 0$ specifies the resonance points. For $|\beta| \ll 1$, equation (2.27) yields

$$K_j \approx {\rm sign}(\beta)\left[(-1)^j r^{1/2} + |\beta|\right] \qquad (|\beta| \ll 1). \quad (2.36)$$

Thus $|K_j| \approx 1$ at $\beta = 0$, and both modes are circularly polarized. In general, at a given density ρ, there are three critical photon energies at which $\beta = 0$. The first is located at $\omega/\omega_{\rm pe} \approx 1 - (\omega_{\rm pe}/\omega_{Be})^2/[2(q+m)]$, i.e., close to $\omega = \omega_{Be}$. We will ignore this critical energy since we are considering only

the $\omega \ll \omega_{Be}$ regime in this paper. The second critical energy is at $\omega = \omega_{Bi}$; this is simply the ion cyclotron resonance and is unrelated to vacuum polarization. The third critical point ("vacuum resonance") is located at [see eqs. (2.31) and (2.32)]

$$v_{\rm e} \approx (q+m)\left(1-\frac{1}{u_{\rm e}}\right)(1-\hat{a}-m) \tag{2.37}$$

or at energy

$$E_{\rm V} = \frac{\hbar\omega_{\rm pe}}{\sqrt{q+m}}\left(1+\frac{1}{2u_{\rm e}}+\frac{\hat{a}+m}{2}\right) \approx \frac{\hbar\omega_{\rm pe}}{\sqrt{q+m}}. \tag{2.38}$$

Note that for $b \ll 3\pi/\alpha_{\rm F}$ ($B \ll 5\times10^{16}$ G), $|\hat{a}|$, $|q|$, $|m| \ll 1$, so that equations (2.37) and (2.38) are good approximations. For $B \ll B_{\rm Q}$, we use equations (2.12)-(2.14) to obtain

$$\begin{aligned} E_{\rm V}(B\ll B_{\rm Q}) &= E_{\rm V}^{(0)} = \left(\frac{15\pi}{\alpha_{\rm F}}\right)^{1/2}\frac{\omega_{\rm pe}}{\omega_{Be}}m_{\rm e}c^2 \\ &= 1.02\,Y_{\rm e}^{1/2}\rho_1^{1/2}B_{14}^{-1}\ {\rm keV}. \end{aligned} \tag{2.39}$$

For $B \gg B_{\rm Q}$, we use the leading terms in equations (2.16) and (2.17) to obtain

$$\begin{aligned} E_{\rm V}(B\gg B_{\rm Q}) &\approx \left(\frac{3\pi}{\alpha_{\rm F}}\right)^{1/2}\left(\frac{B_{\rm Q}}{B}\right)^{1/2}\hbar\omega_{\rm pe} \\ &= 0.69\,Y_{\rm e}^{1/2}\rho_1^{1/2}B_{14}^{-1/2}\ {\rm keV}. \end{aligned} \tag{2.40}$$

For convenience, we define the dimensionless function $f(B)$ via $E_{\rm V} = E_{\rm V}^{(0)}f(B)$, so that

$$f(B) = \frac{E_{\rm V}}{E_{\rm V}^{(0)}} \approx \left(\frac{3\delta_{\rm V}}{q+m}\right)^{1/2}. \tag{2.41}$$

Figure A1 shows that $f(B)$ is a slowly-varying function of b [$f(B) = 1$ for $b \ll 1$ and $f(B) \to (b/5)^{1/2} \approx 0.673\,B_{14}^{1/2}$ for $b \gg 1$; $f(B)$ varies from ≈ 1 at $B_{14} = 1$ to 6.7 at $B_{14} = 100$].

Since $E_{\rm V}$ depends on density, a photon with a given energy E traveling in an inhomogeneous medium encounters the vacuum resonance ($\beta = 0$) at the density

$$\rho_{\rm V} = 0.964\,Y_e^{-1}(B_{14}E_1)^2 f(B)^{-2}\ {\rm g\ cm^{-3}}, \tag{2.42}$$

where $E_1 = E/(1\ {\rm keV})$. In Section 2.4, we discuss how the photon polarization state changes as the photon traverses the resonant density.

2.4 Resonant Conversion of Photon Modes

In Section 2.2, we described the photon modes as the extraordinary mode (X-mode) and ordinary mode (O-mode). This standard way of classifying photon modes (e.g., Mészáros 1992) is useful when $|\beta| \gg 1$: the X-mode has $|K_j| \ll 1$, and its E is mostly perpendicular to the $\hat{k}$-$\hat{B}$ plane; the O-mode has $|K_j| \gg 1$ and is polarized along the $\hat{k}$-$\hat{B}$ plane. The advantage of such a classification is that the X-mode and O-mode interact very differently with matter: the O-mode opacity is largely unaffected by the magnetic field, while the X-mode opacity is significantly reduced (by a factor of order ω^2/ω_{Be}^2) from the zero-field value (see Section 3). However, the X and O-mode classification becomes ambiguous near $|\beta| = 0$ ($|K_j| = 1$). Indeed, equation (2.27) or (2.36) shows that K_j is discontinuous (and changes sign) when crossing through $\beta = 0$ at the resonance density [eq. (2.42)]. This discontinuity in the mode polarization vector can be avoided by adopting a different mode classification scheme: instead of equation (2.27), we define the plus-mode and minus-mode according to

$$K_\pm = \beta \pm \left(\beta^2 + r\right)^{1/2}. \tag{2.43}$$

Clearly, $K_\pm$ are continuous functions of β; the plus-mode always has $K_+ > 0$, and the minus-mode always has $K_- < 0$.

The relationship between the two schemes of mode classification ($j = 1, 2$ for the X and O-modes, and $j = \pm$ for the plus and minus-modes) is illustrated by Figure A2, which shows the values of $K_\pm$ and the refractive indices $n_\pm = ck_\pm/\omega$ for the plus and minus-modes as a function of density near the vacuum resonance for $E = 1$ keV, $B = 5\times10^{14}$ G, and $\theta_B = 45^\circ$ (see Fig. 1 in Paper II for the $B = 10^{14}$ G case; the difference in behavior is due to $E > E_{Bi}$ in Paper II while $E < E_{Bi}$ here). The plus-mode (minus-mode) manifests as the X-mode (O-mode) at high densities but becomes the O-mode (X-mode) at low densities. If the density variation is sufficiently gentle, an X-mode photon created at high densities will remain on the K_+-trajectory as it travels outward and will adiabatically convert into the O-mode after traversing the resonance density. This is analogous to the MSW mechanism for neutrino oscillation (e.g., Bahcall 1989; Haxton 1995). As shown in Paper II, the adiabaticity condition is

$$\gamma_{\rm res} = (E/E_{\rm ad})^3 \gg 1, \tag{2.44}$$

where

$$E_{\rm ad} = 2.52\ [f(B)\tan\theta_B]^{2/3}\,|1-u_{\rm i}|^{1/3}\left(\frac{1\ {\rm cm}}{H_\rho}\right)^{1/3}{\rm keV} \tag{2.45}$$

and $H_\rho = |dz/d\ln\rho|$ is the density scale height along the ray (evaluated at $\rho = \rho_{\rm V}$). For an ionized hydrogen atmosphere, $H_\rho \simeq 2kT/(m_{\rm p}g\cos\theta) = 1.65\,T_6/(g_{14}\cos\theta)$ cm, where $T = 10^6T_6$ K is the temperature, $g = 10^{14}g_{14}$ cm s^{-2} is the gravitational acceleration, and θ is the angle between the ray and the surface normal. The probability of a non-adiabatic "jump" (e.g., from the K_+-curve to the K_--curve) at the resonance is given approximately by the Landau-Zener formula $P_{\rm jump} = \exp(-\pi\gamma_{\rm res}/2)$. Thus, for $E2E_{\rm ad}$, resonant conversion between the X-mode and O-mode is essentially complete; for $E0.5E_{\rm ad}$, a photon will jump across the adiabatic curves (Fig. A2), and an X-mode (O-mode) photon will remain an X-mode (O-mode) photon in passing through the resonance.

Note that the adiabatic, vacuum polarization-induced, resonant mode conversion (from X to O-mode or from O to X-mode) is an intrinsically coherent phenomenon: the distance over which the conversion takes place is much smaller than the photon mean-free path due to absorption or scattering (Paper II). Such mode conversion is clearly different from the incoherent mode-switching due to scattering [see eq. (3.3)], which has been included in previous works (e.g., Pavlov et al. 1995; Özel 2001; Paper I).

As mentioned in Section 1, the formalism of radiative transfer in strong magnetic fields developed so far is inadequate for coping with partial mode conversion at the vacuum resonance. Thus, in this paper, we shall solve the transport equations in the two limiting cases: no mode conversion and

complete mode conversion; these correspond to two different ways of labeling the modes, i.e., X, O-modes with $j = 1, 2$ and plus and minus-modes with $j = \pm$ (see Sections 5 and 6).*

3 BEHAVIOR OF OPACITIES AND VACUUM POLARIZATION RESONANCE

The radiative opacities depend on the normal mode polarization vector through its projection on the rotating frame with the z-axis along $\hat{B}$. The cyclic components of e^j are

$$|e^j_\pm|^2 = \left|\frac{1}{\sqrt{2}}\left(e^j_x \pm i e^j_y\right)\right|^2 = \frac{[1 \pm (K_j \cos\theta_B + K_{z,j}\sin\theta_B)]^2}{2(1+K_j^2+K_{z,j}^2)} \quad (3.1)$$

$$|e^j_z|^2 = \frac{(K_j \sin\theta_B - K_{z,j}\cos\theta_B)^2}{1+K_j^2+K_{z,j}^2}, \quad (3.2)$$

where K_j is given by equation (2.27) for $j = 1, 2$ or equation (2.43) for $j = \pm$, and $K_{z,j}$ is given by equation (2.33).

The electron scattering opacity from mode j ($= 1, 2$ for the X and O-modes or $\pm$ for the plus and minus modes) into mode i is given by (Ventura 1979; Ventura, Nagel, & Mészáros 1979)

$$\kappa^{\rm es}_{ji} = \frac{n_{\rm e}\sigma_{\rm T}}{\rho}\sum_{\alpha=-1}^{1}\frac{\omega^2}{(\omega+\alpha\omega_{Be})^2+\nu_{\rm e}^2}|e^j_\alpha|^2 A^i_\alpha, \quad (3.3)$$

where $n_{\rm e}$ is the electron number density, $\sigma_{\rm T}$ is the Thomson cross-section, and A^i_α is the angle integral given by $A^i_\alpha = (3/8\pi)\int dk\,|e^i_\alpha|^2$. The electron scattering opacity from mode j is

$$\kappa^{\rm es}_{j} = \frac{n_{\rm e}\sigma_{\rm T}}{\rho}\sum_{\alpha=-1}^{1}\frac{\omega^2}{(\omega+\alpha\omega_{Be})^2+\nu_{\rm e}^2}|e^j_\alpha|^2 A_\alpha, \quad (3.4)$$

where $A_\alpha = \sum_{i=1}^2 A^i_\alpha$. In the transverse-mode approximation ($K_{z,j} = 0$), the polarization vector e^j satisfies the completeness relation $\sum_{j=1}^2 |e^j_\pm|^2 = \left(1+\cos^2\theta_B\right)/2$ and $\sum_{j=1}^2 |e^j_z|^2 = \sin^2\theta_B$, and thus $A_\alpha = 1$. For $\omega \ll \omega_{Be}$, a suppression factor $(\omega/\omega_{Be})^2$ in the opacity results from the strong confinement of electrons perpendicular to the magnetic field. Similar features appear in the electron free-free absorption opacity (e.g., Virtamo & Jauho 1975; Pavlov & Panov 1976; Nagel & Ventura 1983)

$$\kappa^{\rm ff,e}_{j} = \frac{\alpha_0}{\rho}\sum_{\alpha=-1}^{1}\frac{\omega^2}{(\omega+\alpha\omega_{Be})^2+\nu_{\rm e}^2}|e^j_\alpha|^2 \bar{g}^{\rm ff}_\alpha, \quad (3.5)$$

where

$$\alpha_0 = 4\pi^2 Z^2 \alpha_{\rm F}^3 \frac{\hbar^2 c^2}{m_{\rm e}^2}\left(\frac{2m_{\rm e}}{\pi kT}\right)^{1/2}\frac{n_{\rm e} n_{\rm i}}{\omega^3}\left(1-e^{-\hbar\omega/kT}\right) = \alpha_0^{\rm ff}\frac{3\sqrt{3}}{4\pi}\frac{1}{\bar{g}^{\rm ff}}, \quad (3.6)$$

$n_{\rm i}$ is the ion number density, and $\alpha_0^{\rm ff}$ and $\bar{g}^{\rm ff}$ are the free-free absorption coefficient and velocity-averaged free-free Gaunt factor, respectively, in the absence of a magnetic field. In equation (3.5), $\bar{g}^{\rm ff}_{\pm 1} = \bar{g}^{\rm ff}_\perp$ and $\bar{g}^{\rm ff}_0 = \bar{g}^{\rm ff}_\parallel$ are the velocity-averaged free-free Gaunt factors in a magnetic field, which we evaluate using the expressions given in Mészáros (1992) (see also Nagel 1980).

The ion contribution to the scattering and absorption opacities are

$$\kappa^{\rm is}_{ji} = \left(\frac{Z^2 m_{\rm e}}{A m_{\rm p}}\right)^2 \frac{n_{\rm i}\sigma_{\rm T}}{\rho}\sum_{\alpha=-1}^{1}\frac{\omega^2}{(\omega-\alpha\omega_{Bi})^2+\nu_{\rm i}^2}|e^j_\alpha|^2 A^i_\alpha \quad (3.7)$$

$$\kappa^{\rm is}_{j} = \left(\frac{Z^2 m_{\rm e}}{A m_{\rm p}}\right)^2 \frac{n_{\rm i}\sigma_{\rm T}}{\rho}\sum_{\alpha=-1}^{1}\frac{\omega^2}{(\omega-\alpha\omega_{Bi})^2+\nu_{\rm i}^2}|e^j_\alpha|^2 A_\alpha \quad (3.8)$$

$$\kappa^{\rm ff,i}_{j} = \frac{1}{Z^3}\left(\frac{Z^2 m_{\rm e}}{A m_{\rm p}}\right)^2 \frac{\alpha_0}{\rho}\sum_{\alpha=-1}^{1}\frac{\omega^2}{(\omega-\alpha\omega_{Bi})^2+\nu_{\rm i}^2}|e^j_\alpha|^2 \bar{g}^{\rm ff}_\alpha. \quad (3.9)$$

Note that the ion cyclotron resonance occurs for $\alpha = +1$, i.e., when the electric field of the mode rotates in the same direction as the ion gyration. The total scattering and absorption opacities in a fully ionized medium is then the sum of the electron and ion components, namely $\kappa^{\rm sc}_j = \kappa^{\rm es}_j + \kappa^{\rm is}_j$ and $\kappa^{\rm abs}_j = \kappa^{\rm ff,e}_j + \kappa^{\rm ff,i}_j$.

In equations (3.3)-(3.9), we have included damping through $\nu_{\rm e} = \nu_{\rm r,e} + \nu_{\rm c,e}$ and $\nu_{\rm i} = \nu_{\rm r,i} + \nu_{\rm c,i}$, where $\nu_{\rm r,e} = (2e^2/3m_{\rm e}c^3)\omega^2$ and $\nu_{\rm r,i} = (Z^2 m_{\rm e}/A m_{\rm p})\nu_{\rm r,e}$ are radiative damping rates and $\nu_{\rm c,e} = (\alpha_0\bar{g}^{\rm ff}_\alpha/n_{\rm e}\sigma_{\rm T})\nu_{\rm r,e}$ and $\nu_{\rm c,i} = (m_{\rm e}/A m_{\rm p})\nu_{\rm c,e}$ are collisional damping rates (see Pavlov et al. 1995, and references therein). For the photon frequencies of interest, $\omega \gg \nu_{\rm e}, \nu_{\rm i}$, and therefore damping is negligible except near resonance.

Figure A3 shows examples of the absorption opacity $\kappa^{\rm abs}_j$ as a function of photon energy for magnetic field $B = 10^{14}$ G and $\theta_B = 45^\circ$ at densities and a temperature characteristic of NS atmospheres. For angles θ_B not too close to 0° or 180° (e.g., $10^\circ\theta_B 170^\circ$), the opacity $\kappa^{\rm abs}_j(\theta_B = 45^\circ)$ is indicative of the behavior of $\kappa^{\rm abs}_j(k)$, while $\kappa^{\rm abs}_j(k)$ exhibits strong angle dependence for θ_B near 0° or 180°. Because of mode conversion due to the vacuum resonance (see Section 2.4), two sets of photon modes are depicted in Fig. A3: when mode conversion is neglected (e.g., an X-mode photon remains in the X-mode when traversing the vacuum resonance), we use $j = 1, 2$ for the X and O-modes (left panels); on the other hand, if we assume that mode conversion is complete for all energies (e.g., a plus-mode photon remains in the plus-mode when crossing the resonance), the opacities are determined with $j = \pm$ (right panels).† Note that since

* In this paper, we are not concerned with possible complications due to mode collapse, which occurs near $\theta_B = 90^\circ$ (see Soffel et al. 1983). It can be shown that the real and imaginary parts of the complex refractive indices of the modes N_j satisfy $\mathrm{Re}|N_+ - N_-| \approx v_{\rm e} u_{\rm e}^{-1/2}|1-u_{\rm i}|^{-1}\cos\theta_B\sqrt{1+\beta^2}$ and $\mathrm{Im}|N_+ - N_-| \approx v_{\rm e}\gamma_{\rm e}\sin\theta_B$ (Paper II), where $\gamma_{\rm e} = \nu_{\rm e}/\omega$ is the dimensionless damping rate of the electron [see eqs. (2.2)-(2.4) and Paper I]. Even at $\beta = 0$, the condition $\mathrm{Re}|N_+ - N_-| \gg \mathrm{Im}|N_+ - N_-|$ is satisfied as long as θ_B is not too close to 90°.

† In plotting the right panels of Fig. A3, we have used $\beta = |\beta_0|\beta_{\rm V}$ [see eqs. (2.29) and (2.30)] in evaluating the polarization parameter β so that the plus or minus-mode is resonant at the ion cyclotron energy. If we use $\beta = \beta_0\beta_{\rm V}$, then the + and − curves

$E_{\rm V}$ depends on ρ, the left and right panels of Fig. A3 represent genuinely different opacities in the radiative transfer (see below).

The behavior of the opacities near the ion cyclotron resonance $E_{Bi} = 0.63\,B_{14}$ keV (for $Z = A = 1$) was studied in Paper I. The vacuum resonance feature at $E_{\rm V}$ [eq. (2.40)] arises from the interplay between the plasma and vacuum polarization effects discussed in Section 2.3 (e.g., Mészáros & Ventura 1979; Pavlov & Shibanov 1979; Ventura, Nagel, & Mészáros 1979). To understand the behavior of the X and O-mode ($j = 1, 2$) opacities near the vacuum resonance, we write the scattering and absorption opacities as

$$\kappa_j^{\rm sc} = \frac{n_{\rm e}\sigma_{\rm T}}{\rho}\xi_j \quad , \quad \kappa_j^{\rm abs} = \frac{\alpha_0}{\rho}\xi_j, \tag{3.10}$$

with

$$\xi_j \approx \left(\frac{1}{u_{\rm e}}|e_+^j|^2 + \frac{1}{u_{\rm e}}|e_-^j|^2 + |e_z^j|^2\right) + \frac{1}{M'^2}$$

$$\times \left[\frac{1}{(1-\sqrt{u_{\rm i}})^2+\gamma_{\rm i}^2}|e_+^j|^2 + \frac{1}{(1+\sqrt{u_{\rm i}})^2}|e_-^j|^2 + |e_z^j|^2\right], \tag{3.11}$$

where $M' = (Am_{\rm p}/Zm_{\rm e})Z^{-1/2}$ for scattering and $M' = (Am_{\rm p}/Zm_{\rm e})Z^{1/2}$ for absorption, $\gamma_{\rm i} = \nu_{\rm i}/\omega$, and we have set the free-free Gaunt factors to unity in $\kappa_j^{\rm abs}$ and $A_\alpha = 1$ in $\kappa_j^{\rm sc}$ for simplicity. Away from the ion cyclotron resonance, the ion contribution to the opacities is negligible, and $\xi_j \approx (|e_+^j|^2 + |e_-^j|^2)/u_{\rm e} + |e_z^j|^2$. In the limit of $|\beta| \gg 1$ (and using the transverse approximation $K_{z,j} \approx 0$ or $v_{\rm e} \ll 1$), we find from equations (2.35), (3.1), and (3.2) that

$$|e_\pm^1|^2 = \frac{1}{2}\left(1 \mp \frac{1}{\beta}\cos\theta_B\right), \quad |e_z^1|^2 = \frac{1}{(2\beta)^2}\sin^2\theta_B \tag{3.12}$$

$$|e_\pm^2|^2 = \frac{1}{2}\cos^2\theta_B\left(1 \pm \frac{1}{\beta\cos\theta_B}\right),$$

$$|e_z^2|^2 = \left[1 - \frac{1}{(2\beta)^2}\right]\sin^2\theta_B. \tag{3.13}$$

Thus, for the X and O-modes,‡

$$\xi_1 \approx \frac{1}{u_{\rm e}} + \frac{1}{4\beta^2}\sin^2\theta_B, \quad \xi_2 \approx \sin^2\theta_B \quad (|\beta| \gg 1). \tag{3.14}$$

On the other hand, in the limit of $|\beta| \ll 1$, we find from equation (2.36) that

$$|e_\pm^j|^2 = \frac{1}{4}\left\{\left[1 \pm (-1)^j \mathrm{sign}(\beta)\cos\theta_B\right]^2 - \left[(-1)^j|\beta| + \frac{\hat{r}}{2}\right]\sin^2\theta_B\right\} \tag{3.15}$$

$$|e_z^j|^2 = \frac{1}{2}\left[1 + (-1)^j\,|\beta| + \frac{\hat{r}}{2}\right]\sin^2\theta_B. \tag{3.16}$$

Thus we have

$$\xi_j \approx \frac{1}{2}\sin^2\theta_B\left[1 + (-1)^j|\beta|\right] \qquad (|\beta| \ll 1). \tag{3.17}$$

will switch across E_{Bi} since β changes sign. However, since E_{Bi} is independent of ρ, it is easy to show that the radiative transfer is the same for both cases ($\beta = |\beta_0|\beta_{\rm V}$ versus $\beta = \beta_0\beta_{\rm V}$).

‡ Note that in this section, we are considering θ_B away from 0 and π; when θ_B is close to 0 or π, the dominant terms in ξ_j are different.

Clearly the X-mode ($j = 1$) opacity is significantly enhanced near the vacuum resonance ($\beta \sim 0$), while the O-mode opacity is only reduced by a factor of two from its usual value. At the resonance, the two modes become circularly polarized and possess the same opacities (see left panels of Fig. A3).

Equations (3.14) and (3.17) determine the "line shape" of the vacuum resonance feature. For $x \equiv (E - E_{\rm V})/E_{\rm V} \ll 1$, equations (2.28)-(2.32) imply $|\beta_{\rm V}| \approx 2|x|$ and

$$|\beta| \approx u_{\rm e}^{1/2}|1-u_{\rm i}||x|\frac{\sin^2\theta_B}{\cos\theta_B} = \frac{|x|}{x_{\rm V}} \tag{3.18}$$

with

$$x_{\rm V} \equiv \frac{\cos\theta_B}{u_{\rm e}^{1/2}|1-u_{\rm i}|\sin^2\theta_B}. \tag{3.19}$$

Thus

$$\xi_X = \xi_1 \approx \begin{cases} \frac{1}{2}\sin^2\theta_B\,(1 - |x|/x_{\rm V}) & |x| \ll x_{\rm V} \\ u_{\rm e}^{-1} + (x_{\rm V}/2x)^2\sin^2\theta_B & x_{\rm V} \ll |x| \ll 1 \end{cases}. \tag{3.20}$$

This should be compared to the value when there is no vacuum polarization (nv),

$$\xi_X^{\rm (nv)} \approx u_{\rm e}^{-1} + x_{\rm V}^2\sin^2\theta_B \sim u_{\rm e}^{-1}. \tag{3.21}$$

The strength of the vacuum resonance feature can be measured by the dimensionless "equivalent width"

$$\Gamma_{\rm V} \equiv \frac{1}{\kappa_X^{\rm (nv)}E_{\rm V}}\int_{\rm res}\kappa_X dE = \frac{1}{\xi_X^{\rm (nv)}E_{\rm V}}\int_{\rm res}\xi_X dE \sim u_{\rm e}\int_{-1/2}^{1/2}\xi_X dx, \tag{3.22}$$

where the integral is over the region in which $\xi_X/\xi_X^{\rm (nv)} > 1$, i.e., $E_{\rm V}/2E3E_{\rm V}/2$ or $-1/2x1/2$ (see Fig. A4). Using equation (3.20) and for $\sin^2\theta_B \sim \cos\theta_B \sim 1$, we find

$$\Gamma_{\rm V} \sim \frac{u_{\rm e}^{1/2}}{|1-u_{\rm i}|} \approx \frac{10^3}{|1-u_{\rm i}|}\left(\frac{1\ \mathrm{keV}}{E}\right)B_{14}. \tag{3.23}$$

It is important to note that the region $|x|$(a few $x_{\rm V}$) $\ll 1$ contributes most to the integral in equation (3.22). This is illustrated by the shaded region in Figure A4, which shows a schematic picture of the vacuum resonance feature; note that from equation (3.20), the continuum is $u_{\rm e}^{-1}$ lower than the peak. This region must be resolved in numerical calculations of atmosphere spectra (see Section 5). Also note that at low densities where $E_{\rm V}$ lies below the ion cyclotron energy so that $u_{\rm i} > 1$, the vacuum resonant feature is narrower [see eq. (3.19); also compare the two left panels in Fig. A3].

When mode conversion is assumed to be complete, the plus and minus-mode opacities $\kappa_\pm$ do not exhibit a line feature but rather show a step function-like change at the vacuum resonance energy $E_{\rm V}$ (see the right panels in Fig. A3).

4 QUALITATIVE DISCUSSION OF THE VACUUM POLARIZATION EFFECT ON ATMOSPHERE EMISSION

In order to understand qualitatively the effects of vacuum polarization on the radiation spectra from magnetar atmospheres, we estimated in Paper II the location of the decoupling layer at which the optical depth is of order unity for photons of different energies and polarization modes. Here

we conduct a somewhat more accurate calculation by including the energy dependence of the Gaunt factor and show results for different magnetic field strengths. For simplicity, we consider fully ionized hydrogen atmospheres, adopt the transverse approximation ($K_{z,j} = 0$), and present results for only $\theta_B = 45^\circ$. We also treat the temperature as a constant, which is a good approximation when estimating the decoupling density since T varies at most by a factor of a few while ρ varies by many orders of magnitude above the decoupling layer. For $g = (GM/R^2)(1-2GM/Rc^2)^{-1/2} = 2.4\times10^{14}$ cm s^{-2} (corresponding to a $M = 1.4\,M_\odot$, $R =$ 10 km NS), hydrostatic equilibrium and the ideal gas equation of state, $P = 2\rho kT/m_{\rm p}$, give the density ρ at column density y (in g cm^{-2}) as $\rho = 1.45\,T_6^{-1}y$ g cm^{-3}, where $T_6 = T/(10^6$ K). The optical depth τ_ν ($= \int \kappa_\nu dy$) at ρ is then given by $\tau_\nu = 0.69\,T_6\int_0^\rho \kappa_\nu\, d\rho'$. Note that we use here the effective opacity defined by $\kappa_\nu = [\kappa_\nu^{\rm abs}(\kappa_\nu^{\rm abs}+\kappa_\nu^{\rm sc})]^{1/2}$ (see Rybicki & Lightman 1979). The decoupling density ρ can then solved for by setting the optical depth $\tau_\nu = 1$. Numerical results of the decoupling density are shown in Figure A5 for $B = 10^{14}$ and 5×10^{14} G.

We can obtain analytic expressions to understand the various features in Fig. A5 by setting the Gaunt factor to unity and by ignoring scattering, which is only important for E10 keV, even though the results shown in Fig. A5 do account for the actual variation of the Gaunt factor and use the effective opacity which includes scattering. First, let us ignore vacuum polarization and proton effects. The absorption opacity can then be written as $\kappa_j^{\rm abs} \approx \kappa_0\xi_j$, where $\kappa_0 \approx 9.3\,\rho_1 T_6^{-1/2}E_1^{-3}S$ cm^{2}g^{-1} [with $S = 1-e^{-E/kT}$, $\rho_1 = \rho/(1$ g cm$^{-3})$, and $E_1 = E/(1$ keV)] is the zero-field opacity and $\xi_O \sim 1$ and $\xi_X \sim u_{\rm e}^{-1}$ [see eqs. (3.10) and (3.14)]. The decoupling densities of the two modes [with no vacuum polarization (nv)] are then approximately

$$\rho_O^{\rm (nv)} \approx 0.56\,T_6^{-1/4}E_1^{3/2}S^{-1/2}\ {\rm g\ cm^{-3}} \quad (4.1)$$

$$\rho_X^{\rm (nv)} \approx u_{\rm e}^{1/2}\rho_O^{\rm (nv)}. \quad (4.2)$$

Thus the X-mode photons emerge from deeper in the atmosphere and are the main carriers of the X-ray flux.

Next, we include vacuum polarization and protons but neglect resonant mode conversion. For the O-mode, the opacity is largely unaffected by the magnetic field and vacuum polarization effect. Thus the decoupling density ρ_O is still $\rho_O^{\rm (nv)}$. For the X-mode, when $\rho_X^{\rm (nv)}\rho_{\rm V}$ or

$$EE_{\rm c2} \approx 77\,T_6^{-1/6}B_{14}^{-2/3}f(B)^{4/3}\ {\rm keV}, \quad (4.3)$$

the photons created at $\rho_X^{\rm (nv)}$ will encounter the vacuum resonance, near which the X-mode opacity is greatly enhanced; thus the decoupling density [with no mode conversion (nc)] $\rho_X^{\rm (nc)}$ will be smaller than $\rho_X^{\rm (nv)}$. For $EE_{\rm c2}$, $\rho_X^{\rm (nc)}$ is close to $\rho_X^{\rm (nv)}$, with the small difference due to the opacity being slightly modified by the vacuum effect even away from the resonance (see the left panels of Fig. A3). To evaluate the X-mode optical depth $\Delta\tau$ across the resonance region (e.g., $0.9 < \rho/\rho_{\rm V} < 1.1$) we note that $\beta \sim u_{\rm e}^{1/2}x$ [eq. (3.18)] for $|x| \equiv |\Delta\rho/\rho_{\rm V}|0.1$. Using equations (3.14) and (3.17), we find $\xi_X \sim 1/(u_{\rm e}x^2)$ for $u_{\rm e}^{-1/2} \ll |x|0.1$ and $\xi_X \sim 1$ for $|x| \ll u_{\rm e}^{-1/2}$ [compare with eq. (3.20)]. We then have $\Delta\tau \sim 0.7\,\kappa_0 T_6\rho_{\rm V}u_{\rm e}^{-1/2} = 6.4\,T_6^{1/2}\rho_{\rm V}^2E^{-3}u_{\rm e}^{-1/2}S$, which is a factor $\sim u_{\rm e}^{1/2}$ larger than the optical depth of the non-resonant region ($\rho 0.9\,\rho_{\rm V}$). Thus at energies below $E_{\rm c2}$, $\rho_X^{\rm (nc)}$ closely follows $\rho_{\rm V}$ until E drops below another critical energy $E_{\rm c1}$, which is set by $\Delta\tau \approx 1$ or

$$E_{\rm c1} \sim 10\,T_6^{-1/4}B_{14}^{-3/2}f(B)^2\ {\rm keV}. \quad (4.4)$$

Below $E_{\rm c1}$, $\rho_X^{\rm (nc)}$ returns to approximately $\rho_X^{\rm (nv)}$ (see Fig. A5).

Now consider the effect of mode conversion at the vacuum resonance. For $E > 1.3\,E_{\rm ad}$ [see eq. (2.45)], adiabatic mode conversion is nearly complete ($P_{\rm jump} < 3\%$). The O-mode photons traveling from high densities through $\rho_{\rm V}$ are converted to X-mode photons, which then freely stream out of the atmosphere. Thus, for $1.3E_{\rm ad} EE_{\rm c2}$, the effective decoupling density for the X-mode is $\rho_X = \rho_{\rm V}$. For $EE_{\rm c2}$, the vacuum resonance occurs inside both the X and O-mode decoupling layers, and therefore $\rho_X \approx \rho_X^{\rm (nv)}$. For $E \ll E_{\rm ad}$, mode conversion is ineffective; therefore $\rho_X = \rho_X^{\rm (nc)}$. Around $E_{\rm ad}$, the X-mode photons are emitted from both $\rho_X^{\rm (nc)}$ (with probability $P_{\rm jump}$) and $\rho_{\rm V}$ [with probability $(1-P_{\rm jump})$]. Also note that $\rho_X^{\rm (nc)} \approx \rho_{\rm V}$ for $EE_{\rm c1}$.

Figure A5 and the above analysis show that vacuum polarization reduces the decoupling density for photons with energies between $\min(E_{\rm c1}, E_{\rm ad})$ and $E_{\rm c2}$, i.e., these photons decouple in shallower, lower temperature regions of the atmosphere. This gives rise to a rather broad depression feature in the emergent radiation between $\min(E_{\rm c1}, E_{\rm ad})$ and $E_{\rm c2}$ (see also Paper II). In other words, even though the vacuum resonance opacity feature is very narrow, it produces a broad depression because of its density dependence and the large density gradient present in NS atmospheres. Clearly, to quantify the depth of the depression, one must solve for the temperature profile of the atmosphere self-consistently (see Sections 5 and 6).

Finally, the sharp absorption feature in Fig. A5 is due to the ion cyclotron resonance at $E_{Bi} = 0.63\,B_{14}$ keV. Previous atmosphere models which neglect vacuum polarization yield relatively large equivalent widths for the proton cyclotron line (Paper I; Zane et al. 2001). However, we see from Fig. A5 that when E_{Bi} lies within the depression trough, i.e., $E_{\rm c1}E_{Bi}E_{\rm c2}$ or 3×10^{14} G $Bf(B)^{-4/5}T_6^{1/10}2\times10^{15}$ G, the continuum flux around E_{Bi} is greatly reduced,[§] and the equivalent width of the ion cyclotron line becomes much narrower (see Section 6.2). This suppression of the ion cyclotron line by vacuum polarization may help to explain the absence of absorption features in the spectra of several AXPs (Juett et al. 2001; Patel et al. 2001; Tiengo et al. 2001).

In Appendix A1, we present a toy atmosphere model that mimics the vacuum resonance effect discussed in this section.

[§] If we use $E_{\rm ad}E_{Bi}$, then the first inequality becomes 4×10^{14} G $Bf(B)^{-2/3}(\tan\theta_B)^{-2/3}$. Note that the range of magnetic fields must be considered very approximate since $E_{\rm c1}$, $E_{\rm ad}$, and $E_{\rm c2}$ depend on the direction of photon propagation, and redistribution of photon spectral flux occurs in real atmospheres. For example, even for $B = 10^{14}$ G, the width of the ion cyclotron line is reduced by vacuum polarization (see Section 6.2).

5 NUMERICAL METHOD FOR TREATING VACUUM POLARIZATION

We solve the full, angle-dependent radiative transfer equations for the two coupled photon modes in order to construct self-consistent NS atmosphere models. Because the method for rigorously treating partial mode conversion has not been developed, we consider two limiting cases: no mode conversion and complete mode conversion at all energies (see Section 2.4). In our models, the temperature corrections $\Delta T(\tau)$ at each Thomson depth τ are applied iteratively until $\Delta T(\tau)/T(\tau)1\%$, deviations from radiative equilibrium are 1%, and deviations from constant flux are 3% (see Paper I for details of our numerical method). Here we discuss the numerical difficulties involved when attempting to include the effects of vacuum polarization in the atmosphere models.

5.1 No Mode Conversion: Grid Resolution

As shown in Section 3, vacuum polarization induces a narrow, density-dependent resonance feature in the X-mode opacities (see Figs. A3 and A4). The "equivalent width" of the vacuum resonance feature at $E_{\rm V}(\rho)$ is dominated by the narrow energy range $\Delta E/E_{\rm V} = |E-E_{\rm V}|/E_{\rm V} 3\,x_{\rm V} \sim u_{\rm e}^{-1/2} \sim 10^{-3}E_1/B_{14}$, where $E_1 = E/(1\ {\rm keV})$. In a real atmosphere, density and energy gradients are smooth so that such a narrow and density-dependent feature is resolved and accounted for completely. Numerical atmosphere models, however, necessarily require finite grids of discrete depth (density), energy, and angle. The difficulty with a finite grid resolution is illustrated in Figure A6. Consider a photon with energy E that happens to lie very close $[|E - E_{\rm V}(\rho_i)|/E_{\rm V}(\rho_i)x_{\rm V}]$ to the vacuum resonance energy $E_{\rm V}(\rho_i)$ of one of the density grid points ρ_i; such a photon will encounter a region of strongly enhanced opacity and will therefore decouple from the matter at a shallow depth. On the other hand, a photon with energy E', which lies outside the resonance regions of all density grid points will not encounter any enhanced opacity regions and will decouple deeper in the atmosphere. Therefore, if we choose a general energy grid that is not tied to the density grid, the computed radiation spectrum will exhibit narrow absorption lines at energies which happen to lie close to $E_{\rm V}$ at one of the density grid points. Such narrow lines are numerical artifacts of the finite grid resolution since, as discussed in Section 4, vacuum polarization is expected to only produce a broad depression in the emission spectrum.

Clearly, to correctly account for the density-dependent vacuum resonance, one must have a depth grid that is sufficiently dense so that the opacity features at neighboring grid points overlap appreciably, i.e., $[E_{\rm V}(\rho_{i+1}) - E_{\rm V}(\rho_i)]/E_{\rm V}(\rho_i)x_{\rm V}$ or $(\rho_{i+1} - \rho_i)/\rho_i u_{\rm e}^{-1/2} \sim 10^{-3}E_1 B_{14}^{-1}$. Such a dense depth grid is beyond the capabilities of the current generation of atmosphere models.

One method to avoid artificial "absorption lines" in the computed spectrum is to adopt an "equal grid" method: we use an equal number of depth (density) and energy grid points with every energy grid point being placed at $E_n = E_{\rm V}(\rho_i)$ (see Fig. A6). The advantage of this method is that it guarantees a smooth spectrum. However, this method has problems as well. In order to determine the atmosphere structure through temperature corrections (see Paper I and references therein), it is necessary to compute mean opacities, which involve integrations over energy, at a given depth; using the "equal grid" method leads to overestimates of the strength of the opacity feature (see Fig. A6: the area under the long-dashed line overestimates the area under the solid line, which represents the true opacity). Nevertheless, by increasing the number of depth grid points, the "equal grid" method will yield atmosphere models increasingly close to reality (see Section 6).

An alternative method to produce smooth spectra involves "saturating" the opacities near the vacuum resonance (Özel 2001). We shall comment on this method in Section 6.3.

5.2 Complete Mode Conversion

If we assume the adiabatic condition given by equation (2.44) is satisfied for all energies, then a plus-mode (minus-mode) photon will remain in the plus-mode (minus-mode) as it traverses the vacuum resonance (see Section 2.4). In this "complete mode conversion" limit, we simply solve the coupled radiative transfer equations for the plus and minus-mode photons rather than the X and O-mode photons. The numerical procedure is analogous to the one outlined in Paper I. The modes are calculated using equation (2.43) for the polarization parameter rather than equation (2.27). In this case, the vacuum resonance manifests as a step function-like feature in the opacities, as discussed in Section 3 and shown in the right panels of Fig. A3, and there is no numerical difficulty in handling such an opacity feature.

6 NUMERICAL RESULTS

6.1 Atmosphere Structure

The temperature profiles for fully ionized hydrogen atmospheres with $T_{\rm eff} = 5 \times 10^6$ K and magnetic field $B = 5\times10^{14}$ G oriented perpendicular to the surface (i.e., the angle between the field and the surface normal is $\Theta_B = 0$) are plotted in Figure A7. The curves marked "nc#" are models which include vacuum polarization but no mode conversion and using the equal grid method described in Section 5.1, with the "#" indicating the number of grid points per decade in Thomson depth τ. When vacuum polarization is neglected (nv), the temperature profiles show a plateau at $\tau \sim 1 - 100$ (such a feature was already noted in Paper I[¶] and in Özel 2001[‖]). This arises because the X-mode photons decouple at $\tau \sim$ a few $\times 10^2$ and thus have very little energy exchange with the matter, while for τ1, the O-mode photons are ineffective at regulating the temperature because of their small flux. We see from Fig. A7 that vacuum

[¶] The "no vacuum polarization" models presented here differ slightly from those in Paper I because of a numerical error in our calculation of the Gaunt factors in Paper I. This error has been corrected in the present paper.

[‖] Özel's models include vacuum polarization; see Section 6.3.

polarization tends to diminish this plateau in the temperature profile since vacuum polarization causes the X and O-mode opacities to be similar to each other (see Fig. A3) and the decoupling densities to be closer (see Fig. A5). We also see that vacuum polarization tends to increase the temperature at most depths (and the general temperature gradient) relative to the case without vacuum polarization. In the deepest layers where both modes are diffusing, a rise in the X-mode opacity due to the vacuum resonance feature reduces the bandwidth over which flux can be transported, and a larger temperature gradient is required to maintain a constant total flux; these layers are therefore backwarmed to higher temperatures (see Mihalas 1978 for a general discussion of backwarming). On the other hand, in the plateau $\tau \sim 1 - 100$, the free streaming X-mode photons, generated from deeper, hotter layers, encounter a sharp rise in opacity and are absorbed, which causes the temperature to increase.

Figure A8 compares the temperature versus density profiles for various magnetic fields and vacuum polarization effects. For the models which include vacuum polarization but neglect mode conversion (nc), we use twenty grid points per decade in τ. Compared to models without vacuum polarization (nv), the models with complete mode conversion (mc) show higher temperatures in the deep layers: although the O-mode photons at a particular depth are converting into X-mode photons and carrying away heat, X-mode photons from deeper, hotter layers are converting into O-mode photons and depositing more energy. We also note that larger magnetic fields cause the vacuum resonance to occur at a lower energy for a given density or at a higher density for a given energy [see eqs. (2.39), (2.40), and (2.42)] and thus shift the region that is heated by vacuum polarization effects to deeper layers.

In Appendix A1, we construct toy atmosphere models with opacities which mimic the vacuum polarization effect. The temperature profiles of the toy models are qualitatively similar to the results discussed in this section.

6.2 Spectra

Figure A9 shows the spectra of fully ionized hydrogen atmospheres with $B = 5 \times 10^{14}$ G, $\Theta_B = 0$ (magnetic field perpendicular to stellar surface), and $T_{\rm eff} = 5 \times 10^6$ K. Plotted alongside is the blackbody spectrum at $T = 5 \times 10^6$ K. This figure illustrates the effect of grid resolution for models which include vacuum polarization but no mode conversion. As discussed in Section 5.1, a lower grid resolution tends to overestimate the strength of the vacuum resonance feature, which leads to the stronger depression at $\sim 0.2 - 2$ keV. In the following, we shall use the "nc20" model when we show results which include vacuum polarization but no mode conversion and adopt the abbreviation "nc".

Figures A10-A12 depict the spectra for fully ionized hydrogen atmosphere models with $B = 10^{14}$ G, 5×10^{14} G, and 10^{15} G, respectively, $\Theta_B = 0$, and $T_{\rm eff} = 5 \times 10^6$ K. In each figure, the spectra from three models are depicted together with a blackbody spectrum at $T = 5 \times 10^6$ K: a model which neglects vacuum polarization (nv), a model which includes vacuum polarization but no mode conversion (nc), and a model which assumes complete vacuum polarization-induced mode conversion (mc). Recall that the nc model and the mc model represent two limiting cases, and the true results with partial mode conversion (see Section 2.4) are expected to lie between the nc and mc curves. We see from Figs. A10-A12 that the differences in the spectra between the two limiting cases are not significant.

Figures A10-A12 show that, when vacuum polarization is neglected (nv), the spectra exhibit significantly harder high energy tails and a depletion of low energy photons relative to the blackbody. The hard tails were already noted in previous studies of NS atmospheres with $B 10^{13}$ G (e.g., Shibanov et al. 1992; Pavlov et al. 1995; see also references cited in Paper I), and they arise because high energy photons have lower opacities and thus decouple from deeper, hotter layers. We see from Figs. A10-A12 that vacuum polarization can significantly reduce these high energy tails (E a few keV) and causes the spectra to be softer compared to the models without vacuum polarization. This reduction of the high energy tail is due to the broad depression caused by the density-dependent vacuum resonance feature, as discussed in Section 4 (see Fig. A5).

Figures A10-A12 also reveal that vacuum polarization can significantly suppress the ion cyclotron line feature in the spectra. When vacuum polarization is neglected, the ion cyclotron line is broad (see Paper I for more discussion of the feature; see also Zane et al. 2001), and the equivalent widths are 0.14 keV ($E_{Bi} = 0.63$ keV), 2 keV ($E_{Bi} = 3.15$ keV), and 4 keV ($E_{Bi} = 6.3$ keV) for $B_{14} = 1$, 5, and 10, respectively. When vacuum polarization is included but mode conversion is neglected (model nc), the equivalent widths become 20 eV ($E_{Bi} = 0.63$ keV), 0.1 keV ($E_{Bi} = 3.15$ keV), and 0.2 keV ($E_{Bi} = 6.3$ keV), i.e., the equivalent widths of the ion cyclotron line have been reduced by a factor of ~ 10; when mode conversion is assumed to be complete (model mc), the equivalent widths are even smaller: 8 eV ($E_{Bi} = 0.63$ keV), 0.09 keV ($E_{Bi} = 3.15$ keV), and 0.05 keV ($E_{Bi} = 6.3$ keV), i.e., a reduction by a factor > 10. This reduction of the ion cyclotron line strength by vacuum polarization was expected from the analysis in Section 4 (see Fig. A5), and it occurs when the ion cyclotron energy E_{Bi} overlaps with the broad depression caused by the vacuum resonance. The reduced width of the ion cyclotron line makes the line difficult to observe with current X-ray detectors; this may help to explain the absence of line features in recent X-ray observations of several magnetar candidates (Juett et al. 2001; Patel et al. 2001; Tiengo et al. 2001).

A comparison of the spectra for the models with different magnetic fields is shown in Figure A13 for the case which includes vacuum polarization but no mode conversion (nc) and in Figure A14 for the case which includes vacuum polarization with complete mode conversion (mc). Note that despite the suppression of the high energy tails by the vacuum polarization effect, all spectra are still harder than the blackbody spectrum.

6.3 Comparison with Previous Work

As mentioned in Section 1, there have been few previous works on magnetar atmosphere models that include the effect of vacuum polarization. The most recent and relevant one is that by Özel (2001), who constructed self-consistent atmosphere models with parameters similar to those de-

scribed in our paper, i.e., $T_{\rm eff} \sim 5\times10^6$ K, $B \sim 10^{14}-10^{15}$ G, $\Theta_B = 0$, and the atmosphere consists of fully ionized hydrogen. While there are qualitative resemblances between some aspects of our results and Özel's, e.g., the temperature profiles show plateau features which are weakened by vacuum polarization (compare our Fig. A7 to her Fig. 5), there are also major differences in the physical ingredients and methods used in our models and those of Özel's. (1) Özel applied the vacuum polarization formulae which are valid only for $BB_{\rm Q} = 4.4 \times 10^{13}$ G. At $B10^{15}$ G, these incorrect formulae underestimate the vacuum resonance energy by a factor of a few (see Fig. A1). (2) Özel neglected ions in the plasma response and the ion cyclotron resonance in the opacities. As discussed in Paper I, the ion effects cannot be neglected since they influence the spectrum in the same energy range as vacuum polarization effects. Figure A15 compares the spectra of atmosphere models which include ions and neglects ions. Despite the suppression of the ion cyclotron feature by the vacuum polarization effect (Section 6.2), the "with ion" and "no ion" cases have appreciably different spectra (e.g., at $E = 10$ keV, the flux of model "nc" differs from model "nc/no ions" by a factor of about ten). (3) Özel's work neglects the recently discovered mode conversion effect due to vacuum polarization (Paper II; Section 2.4). (4) Even when mode conversion is neglected, Özel's method of treating the vacuum resonance differs from ours. As discussed in Section 5.1, to fully account for the density-dependent vacuum resonance feature in the opacity (and thus producing smooth spectra), one would need to have a prohibitively high density/depth grid resolution. Özel produces smooth spectra by adopting a "saturation" method, whereby the peak X-mode opacity is restricted by requiring $|\beta_{\rm V}| \geq 0.01$ [see eqs. (2.32) and (3.18); recall that the vacuum resonance occurs at $\beta_{\rm V} = 0$]. However, as discussed in Section 3, the region with $|\beta_{\rm V}| \sim |E/E_{\rm V} - 1| x_{\rm V} \sim u_{\rm e}^{-1/2}$ [~ 0.001 at 1 keV for $B = 10^{14}$ G; see eq. (3.19) and Fig. A4] contributes most to the "equivalent width" of the vacuum resonance feature. Therefore the saturation method does not capture the main contribution of the vacuum resonance feature in the opacities and significantly underestimates the effect of vacuum polarization. Figure A7 shows the temperature profile of the atmosphere model using our "equal grid" method together with the restriction $|\beta_{\rm V}| \geq 0.01$. Clearly, since the saturation scheme does not capture the entire effect of the opacity change, the heating of the atmosphere (compared to the case in which vacuum polarization is neglected) due to the vacuum resonance feature is less than the model with no saturation restriction. Figure A16 compares the spectra with and without saturation. Two effects are responsible for the qualitative differences. First, because saturation underestimates the "equivalent width" of the vacuum resonance feature, it does not yield the true decrease in flux (see Section 4) so that the the broad depression does not reach as low of energies. Second, the softer spectra of the saturation model at energies $E1$ keV is the result of the lower temperature at the photon decoupling layers in this model (see Fig. A7). We also note again that even though vacuum polarization produces harder spectra at high energies than the blackbody spectrum at the same effective temperature, the spectra are still softer than atmosphere models which neglect vacuum polarization (see Figs. A10-A12).

It is appropriate to reiterate that our own numerical treatment of the vacuum polarization effect also has limitations, and these are discussed in Section 5. We also note that Özel's calculations include the full angular dependence of the scattering opacity, whereas the results presented in this paper are based upon an approximate calculation of the scattering source function in order to speed up the computation (see Section 2.2 of Paper I). Our numerical tests show that this approximation does not affect the temperature profile of the atmosphere and only produces a small reduction (by less than a factor of two) in the flux at very high energies ($E10$ keV). Finally, we have not examined the angular dependence and beaming pattern of the emission as done in Özel (2001) (see also Özel, Psaltis, & Kaspi 2001 and Özel 2002 for analyses of the resulting pulse profiles and pulse fractions).

7 DISCUSSION AND CONCLUSION

We have presented a detailed study on the atmospheres and thermal radiation of isolated neutron stars with superstrong magnetic fields $B \geq 10^{14}$ G and effective temperatures $T_{\rm eff} \sim$ a few $\times\, 10^6$ K. Such a study is needed since surface emission has already been detected from a number of magnetar candidates (AXPs and SGRs), and current/future observations, when combined with theoretical modeling, can potentially provide important constraints on the properties of these enigmatic objects (see Section 1).

Following up our previous work on magnetized neutron star atmospheres (Paper I), we focus on the effect of vacuum polarization in this paper. It was already known from earlier theoretical studies (see Section 1 and Mészáros 1992 for references), which we have generalized to the $B10^{14}$ G regime and included the effect of ions, that vacuum polarization changes the dielectric property of the plasma and gives rise to a resonance feature in the opacity at photon energy $E_{\rm V} \approx 1.02\, Y_{\rm e}^{1/2} \rho_1^{1/2} B_{14}^{-1} f(B)$ keV, where $Y_{\rm e} = Z/A$ is the electron fraction, $\rho_1 = \rho/(1\ {\rm g\ cm^{-3}})$, $B_{14} = B/(10^{14}\ {\rm G})$, and $f(B)$ is a slowly-varying function of B of order unity (see Fig. A1). More recently, it was shown (Paper II) that photons with energies E a few keV propagating in the atmospheric plasma can adiabatically convert from one polarization mode into another at the vacuum resonance density $\rho_{\rm V} \approx 0.96\, Y_{\rm e}^{-1} E_1^2 B_{14}^2 f(B)^{-2}$ g cm^{-3}, where $E_1 = E/(1\ {\rm keV})$; this resonant mode conversion greatly influences the radiative transport because the two modes have vastly different opacities in strong magnetic fields. In this paper, we have attempted to incorporate these vacuum polarization effects into self-consistent atmosphere models. Through both analytic considerations (Section 4; see also Paper II) and numerical calculations (Section 6), we have shown that vacuum polarization leads to a broad depression in the high-energy (E a few keV) radiation flux from the atmospheres as compared to models without vacuum polarization. Despite the rather sharp vacuum resonance feature in the opacity at a given density, the depression in the spectrum is broad (from a few keV to tens of keV, depending on the field strength) because of the large density gradient in the atmosphere. As

a result, the atmosphere emissions possess softer high energy tails than models without vacuum polarization**.

Another important effect of vacuum polarization on the atmospheric spectra is that the strength of the ion cyclotron line is greatly suppressed when vacuum polarization is included in the atmosphere models (see Figs. A10-A12). This is a direct consequence of the aforementioned flux depression caused by vacuum polarization (see Fig. A5): when the depression trough overlaps with the ion cyclotron line at $E_{Bi} = 0.63\, Y_e B_{14}$ keV, i.e., for 10^{14} G$B 5 \times 10^{15}$ G, the continuum flux around E_{Bi} is greatly reduced, and the ion cyclotron line appears narrower (see Section 4). For example, we find that the equivalent width of the 3.15 keV proton cyclotron line for $B = 5 \times 10^{14}$ G is reduced from about 2 keV (no vacuum polarization) to about 0.1 keV (with vacuum polarization). Obviously the reduction of the ion cyclotron line width makes the line more difficult to detect. Indeed, recent observations of several AXPs with *Chandra* and *XMM-Newton* X-ray telescopes failed to reveal any significant line features in the spectra (e.g., Juett et al. 2001; Patel et al. 2001; Tiengo et al. 2001)††.

We note that the radiative transport formalism adopted in this paper (and in previous atmosphere models by other researchers) relies on the transfer of two photon polarization modes. This is inadequate for treating the vacuum polarization-induced resonant mode conversion effect, especially because the effectiveness of mode conversion depends on photon energy (see Section 2.4 and Paper II). The atmosphere models studied in this paper represent two limiting solutions to the transfer problem (no mode conversion and complete mode conversion), and they are expected to bracket the true solution. Nevertheless, to properly account for the mode conversion effect associated with vacuum polarization, one must go beyond the modal description of the radiation field by formulating and solving the transfer equation in terms of the photon density matrix (or Stokes parameters) and including the effect of a nontrivial refractive index. This remains an important problem to be studied in the future.

We caution that our models, as well as previous models of magnetar atmospheres (see Section 1), assume that the atmospheres are completely ionized. For the magnetic field strengths and surface temperatures characteristic of AXPs and SGRs, it is not clear that bound atoms and molecules have sufficiently small abundances to contribute negligibly to the opacity (see the discussion section in Paper I), given their greatly enhanced binding energies in strong magnetic fields (see Lai 2001 for a review). Also of concern is the dense plasma effect on the radiative transfer (see Paper I). Clearly, much work remains to be done before we can have complete confidence in our quantitative understanding of the radiation from the surfaces of strongly magnetized neutron stars.

** For all the models studied here, the spectra are still harder than the blackbody spectrum (with the same effective temperature) because of the non-grey opacities. Also note that in this paper we are only concerned with thermal emission from the neutron star surface. Nonthermal emission or the reprocessing of the thermal emission by the magnetospheric plasma may give rise to high energy, power-law tails in the magnetar spectra (e.g., Thompson, Lyutikov, & Kulkarni 2001).

†† For AXP 4U0142+61, Juett et al. (2001) give an upper limit of about 50 eV for the equivalent width of any line feature in the spectrum; this is larger than our predicted value of $\sim 8 - 20$ eV at $B = 10^{14}$ G and comparable to our value of ~ 100 eV at $B = 5 \times 10^{14}$ G. In addition, it should be noted that the spectra presented in our paper correspond to emission from a local patch of the neutron star surface. When the spectra are integrated over the entire observable surface, which necessarily involves (very uncertain) variations in the magnetic field strength and direction and effective temperature, the equivalent width of the cyclotron line will be further reduced.

Acknowledgments

We thank Tomasz Bulik, Jeremy Heyl, Feryal Özel, Alex Potekhin, Roberto Turolla, Ira Wasserman, and Silvia Zane for useful discussion and correspondence. This work is supported in part by NASA grant NAG 5-8484 and NSF grant AST 9986740. W.C.G.H. is also supported by a fellowship from the NASA/New York Space Grant Consortium, and D.L. is also supported by a fellowship from the A.P. Sloan Foundation.

REFERENCES

Adler, S.L. 1971, Ann. Phys., 67, 599
Bahcall, J. 1989, Neutrino Astrophysics (Cambridge: Cambridge University Press)
Becker, W. 2000, in Proc. IAU Symp. 195, Highly Energetic Physical Processes and Mechanisms for Emission from Astrophysical Plasmas (San Francisco: ASP), p.49
Bezchastnov, V.G., Pavlov, G.G., Shibanov, Yu.A., & Zavlin, V.E. 1996, in Gamma-Ray Bursts, AIP Conf. Proc. Ser. vol. 384, eds. Kouveliotou, C., Briggs, M.F., Fishman, G.J. (NY: AIP), p. 907
Bulik, T. & Miller, M.C. 1997, MNRAS, 288, 596
Gnedin, Yu.N., Pavlov, G.G., & Shibanov, Yu.A. 1978, Sov. Astron. Lett., 4, 117
Haxton, W.C. 1995, ARAA, 33, 459
Heyl, J.S. & Hernquist, L. 1997a, J. Phys. A, 30, 6485
Heyl, J.S. & Hernquist, L. 1997b, Phys. Rev. D, 55, 2449
Ho, W.C.G. & Lai, D. 2001, MNRAS, 327, 1081 (Paper I)
Hurley, K. 2000, in Gamma-Ray Bursts: Fifth Huntsville Symposium, AIP Conf. Proc. 526, eds. Kippen, R.M., Mallozzi, R.S., & Fishman, G.J. (New York: AIP), p. 763
Israel, G., Mereghetti, S., & Stella, L. 2001, review presented at "Soft Gamma-ray Repeaters: Rome 2000 Mini-Workshop" (astro-ph/0111093)
Juett, A.M., Marshall, H.L., Chakrabarty, D., Canizares, C.R., & Schulz, N.S. 2001, in Neutron Stars in Supernova Remnants, ASP Conf. Proc., eds. Slane, P.O., Gaensler, B.M., in press (astro-ph/0111507)
Lai, D. 2001, Rev. Mod. Phys., 73, 629
Lai, D. & Ho, W.C.G. 2002, ApJ, 566, in press (Paper II) (astro-ph/0108127)
Mereghetti, S. 1999, in NATO ASI Neutron Star-Black Hole Connection, eds. Kouveliotou, C., van Paradijs, J., Ventura, J. (Dordrecht: Kluwer), in press (astro-ph/9911252)
Mészáros, P. 1992, High-Energy Radiation from Magnetized Neutron Stars (Chicago: University of Chicago Press)
Mészáros, P. & Ventura, J. 1979, Phys. Rev. D, 19, 3565
Mihalas, D. 1978, Stellar Atmospheres (2d ed.; San Francisco: W.H. Freeman and Co.)
Nagel, W. 1980, ApJ, 236, 904

Nagel, W. & Ventura, J. 1983, A&A, 118, 66
Özel, F. 2001, ApJ, 563, 276
Özel, F. 2002, ApJ, submitted (astro-ph/0201158)
Özel, F., Psaltis, D., & Kaspi, V.M. 2001, ApJ, 563, 255
Patel, S.K., et al. 2001, ApJL, 563, L45
Pavlov, G.G. & Gnedin, Yu.N. 1984, Sov. Sci. Rev. E, 3, 197
Pavlov, G.G. & Panov, A.N. 1976, Sov. Phys. JETP, 44, 300
Pavlov, G.G. & Shibanov, Yu.A. 1979, Sov. Phys. JETP, 49, 741
Pavlov, G.G., Sanwal, D., Garmire, G.P., & Zavlin, V.E. 2001, in Neutron Stars in Supernova Remnants, ASP Conf. Proc., eds. Slane, P.O., Gaensler, B.M., in press (astro-ph/0112322)
Pavlov, G.G., Shibanov, Yu.A., Zavlin, V.E., & Meyer, R.D. 1995, in Lives of the Neutron Stars, eds. Alpar, M.A., Kiziloglu, U., & van Paradijs, J. (Boston: Kluwer Academic), p.71
Perna, R., Heyl, J.S., Hernquist, L.E., Juett, A.M., & Chakrabarty, D. 2001, ApJ, 557, 18
Rybicki, G.B. & Lightman, A.P. 1979, Radiative Processes in Astrophysics (New York: John Wiley & Sons)
Shafranov, V.D. 1967, in Reviews of Plasma Physics, vol. 3, ed. M.A. Leontovich (New York: Consultants Bureau)
Shibanov, Yu.A., Zavlin, V.E., Pavlov, G.G., & Ventura, J. 1992, A&A, 266, 313
Soffel, M., Ventura, J., Herold, H., Ruder, H., & Nagel, W. 1983, A&A, 126, 251
Thompson, C. 2000, in NATO ASI Neutron Star-Black Hole Connection, eds. Kouveliotou, C., van Paradijs, J., Ventura, J. (Dordrecht: Kluwer), in press (astro-ph/0010016)
Thompson, C. & Duncan, R.C. 1996, ApJ, 473, 322
Thompson, C., Lyutikov, M., & Kulkarni, S.R. 2001, ApJ, submitted (astro-ph/0110677)
Tiengo, A., Goehler, E., Staubert, R., & Mereghetti, S. 2001, A&A, in press (astro-ph/0111304)
Treves, A., Turolla, R., Zane, S., & Colpi, M. 2000, PASP, 112, 297
Tsai, W.Y. & Erber, T. 1975, Phys. Rev. D, 12, 1132
Ventura, J. 1979, Phys. Rev. D, 19, 1684
Ventura, J., Nagel, W., & Mészáros, P. 1979, ApJL, 233, L125
Virtamo, J. & Jauho, P. 1975, Nuovo Cimento B, 26, 537
Zane, S., Turolla, R., Stella, L., & Treves, A. 2001, ApJ, 560, 384

APPENDIX A1: ATMOSPHERE INCLUDING VACUUM POLARIZATION RESONANCE EFFECTS: TOY MODELS

A1.1 Opacities

In Section 4, we examined the effect of the vacuum polarization resonance feature on the depth at which the photons that comprise the surface spectrum are emitted. To determine the emission spectrum, the temperature profile must be determined self-consistently. In this section, we consider several toy atmosphere models based on the simplified opacities shown in Figure A17. These models serve to illustrate the key physical effects of the vacuum resonance feature and the numerical subtleties when constructing real atmosphere models (Sections 5 and 6).

As shown in Section 3, in a real atmosphere, the O-mode ($j = 2$) opacity is largely unaffected by the vacuum resonance while the X-mode ($j = 1$) opacity exhibits a significant peak around $E_{\rm V}$. Therefore, for Model (a), we assume the O-mode opacity is grey, $\kappa_{\rm E}^{O} = \kappa_{\rm H}$, and the X-mode opacity has a simple square function form:

$$\kappa_{\rm E}^{X} = \begin{cases} \kappa_{\rm L} & \text{for } E < E_{\rm V} \text{ or } E > \lambda E_{\rm V} \\ \kappa_{\rm H} & \text{for } E_{\rm V} \le E \le \lambda E_{\rm V} \end{cases} \quad \text{[Model (a)]}, \quad \text{(A1)}$$

where

$$E_{\rm V} = \zeta \rho^{1/2}, \quad \text{(A2)}$$

ρ is in g cm^{-3}, E is in keV, $\zeta \approx B_{14}^{-1} f(B)$ [see eqs. (2.39)-(2.41)], and the width of the line feature is $(\lambda - 1)E_{\rm V}$. Equation (A1) thus resembles the X-mode opacity shown in the left panels of Fig. A3 near the vacuum polarization resonance. From Section 3, we know that $\kappa_{\rm H}/\kappa_{\rm L} \sim u_{\rm e}$ at the resonance peak, and the width is $(\lambda - 1) \sim (u_{\rm e}^{1/2}|1 - u_{\rm i}|)^{-1}$; we will see that only the "equivalent width" $(\kappa_{\rm H}/\kappa_{\rm L})(1 - \lambda^{-2}) \sim u_{\rm e}^{1/2}/|1 - u_{\rm i}|$ ($\sim 10^3$ at 1 keV for $B = 10^{14}$ G) matters for the radiation spectrum. Model (a) mimics the real atmosphere models where vacuum-induced mode conversion is neglected.

In Model (b), we assume the plus and minus-mode opacities are simple step functions:

$$\kappa_{\rm E}^{+} = \begin{cases} \kappa_{\rm H} & \text{for } E < E_{\rm V} \\ \kappa_{\rm L} & \text{for } E \ge E_{\rm V} \end{cases} \quad \text{[Model (b)]}$$

$$\kappa_{\rm E}^{-} = \begin{cases} \kappa_{\rm L} & \text{for } E < E_{\rm V} \\ \kappa_{\rm H} & \text{for } E \ge E_{\rm V} \end{cases} \quad \text{[Model (b)]}. \quad \text{(A3)}$$

These opacities resemble the behavior of the plus and minus-modes in the right panels of Fig. A3. Thus Model (b) mimics the atmospheres where mode conversion is assumed to be complete.

A1.2 Photon-Matter Decoupling Region

As in Section 4, we can calculate the density $\rho_{\rm d}$ where photons of different modes decouple from the matter. The corresponding decoupling depth $\tau_{\rm d}(E)$ is determined from $1 = \int_0^{\tau_{\rm d}} d\tau_L [\kappa_{\rm E}(\tau_L)/\kappa_{\rm L}]$, where $d\tau_L = -\rho \kappa_{\rm L}\, dz$. Similar to Section 4, we assume a constant temperature profile when calculating $\tau_{\rm d}$ and $\rho_{\rm d}$ (see Section 4 for justification). Thus, for a fully ionized hydrogen atmosphere, $\rho(\tau_L) = 1.45\, y T_6^{-1} = \rho_0 \tau_L T_6^{-1}$ g cm^{-3}, where $\rho_0 \approx 1.45/\kappa_{\rm L}$ (here $\kappa_{\rm L}$ is in cm^{2}g^{-1} and ρ_0 is in g cm^{-3}). Combining the density profile with equation (A1) gives the X-mode opacity as a function of τ_L, i.e., $\kappa_{\rm E}(\tau_L) = \kappa_{\rm H}$ for $(T_6/\rho_0)(E/\lambda\zeta)^2 \le \tau_L \le (T_6/\rho_0)(E/\zeta)^2$ and $\kappa_{\rm E}(\tau_L) = \kappa_{\rm L}$ otherwise. We then obtain the decoupling depth $\tau_{\rm d}$ of the X-mode as a function of energy,

$$\tau_{\rm d}(E) = \begin{cases} 1 - (\kappa_{\rm H}/\kappa_{\rm L} - 1)\left(1 - \lambda^{-2}\right) \rho_0^{-1} T_6 \left(E/\zeta\right)^2 \\ \qquad \text{for } E < E_{\rm c1} \\ \kappa_{\rm L}/\kappa_{\rm H} + (1 - \kappa_{\rm L}/\kappa_{\rm H})\, \rho_0^{-1} T_6 \left[E/\left(\zeta\lambda\right)\right]^2 \\ \qquad \text{for } E_{\rm c1} \le E \le E_{\rm c2} \\ 1 \qquad \text{for } E > E_{\rm c2} \end{cases} \quad \text{(A4)}$$

The two critical energies, $E_{\rm c1}$ and $E_{\rm c2}$, corresponding to when the decoupling depth $\tau_{\rm d} = (T_6/\rho_0)(E/\zeta)^2$ and $\tau_{\rm d} = (T_6/\rho_0)(E/\lambda\zeta)^2$ are

$$E_{\rm c1} = \zeta \rho_0^{1/2} T_6^{-1/2} \lambda \left[1 + \frac{\kappa_{\rm H}}{\kappa_{\rm L}}\left(\lambda^2 - 1\right)\right]^{-1/2} \quad \text{(A5)}$$

$$E_{\rm c2} = \zeta \rho_0^{1/2} T_6^{-1/2} \lambda. \quad \text{(A6)}$$

The decoupling density, $\rho_{\rm d} = \rho(\tau_{\rm d})$, is given by

$$\rho_{\rm d}(E) = \begin{cases} \rho_0 T_6^{-1} - (\kappa_{\rm H}/\kappa_{\rm L} - 1)\left(1-\lambda^{-2}\right)(E/\zeta)^2 \\ \qquad \text{for } E < E_{\rm c1} \\ \rho_0 T_6^{-1}\kappa_{\rm L}/\kappa_{\rm H} + (1-\kappa_{\rm L}/\kappa_{\rm H})\left[E/\left(\zeta\lambda\right)\right]^2 \\ \qquad \text{for } E_{\rm c1} \le E \le E_{\rm c2} \\ \rho_0 T_6^{-1} \qquad \text{for } E > E_{\rm c2} \end{cases} . \quad \text{(A7)}$$

Note that when $\kappa_{\rm L}/\kappa_{\rm H} \ll 1$ and $\lambda \approx 1$, the decoupling density $\rho_{\rm d}(E) \approx (E/\zeta)^2 = \rho_{\rm V}(E)$ for $E_{\rm c1} \le E \le E_{\rm c2}$, which is in agreement with the result of Section 4 (see Fig. A5). Equations (A4) and (A7) are plotted in Figure A18 with $\zeta = 0.3$, $\lambda = 1.3$, $\kappa_{\rm H} = \kappa_0^{\rm es} = 0.4$ cm^2 g^{-1}, and $\kappa_{\rm L} = 10^{-4}\kappa_0^{\rm es}$; the choice of these parameter values is discussed in Section A1.3. The minimum decoupling depth and density occur at $E_{\rm c1}$:

$$\tau_{\rm d}(E_{\rm c1}) = \frac{1}{\lambda^{-2} + \kappa_{\rm H}/\kappa_{\rm L}\,(1-\lambda^{-2})} \quad \text{(A8)}$$

$$\rho_{\rm d}(E_{\rm c1}) = \frac{\rho_0 T_6^{-1}}{\lambda^{-2} + \kappa_{\rm H}/\kappa_{\rm L}\,(1-\lambda^{-2})}. \quad \text{(A9)}$$

Clearly the minimum decoupling depth depends critically on the equivalent width of the opacity feature, i.e., $(\kappa_{\rm H}/\kappa_{\rm L})(1-\lambda^{-2})$, which corresponds to $\Gamma_{\rm V}$ in equation (3.22). In fact, in the limit of $\kappa_{\rm L}/\kappa_{\rm H} \ll 1$ and $\lambda \approx 1$, the parameters $\kappa_{\rm L}$, $\kappa_{\rm H}$, and λ enter equations (A4)-(A9) only through the combination $(\kappa_{\rm H}/\kappa_{\rm L})(1-\lambda^{-2})$. The larger the equivalent width, the shallower the decoupling depth and hence the cooler the region where the observable photons are produced and the deeper the depression that is produced in the emission spectrum. Also, equations (A5) and (A6) show that, by increasing the magnetic field (or decreasing ζ), the broad depression is shifted to lower energies.

Now consider Model (b) with opacities given by equation (A3). Using the same procedure as above, we obtain the decoupling densities for the plus and minus-mode:

$$\rho_{\rm d}^{+}(E) = \begin{cases} \rho_0 T_6^{-1}\kappa_{\rm L}/\kappa_{\rm H} + (1-\kappa_{\rm H}/\kappa_{\rm L})\,(E/\zeta)^2 \\ \qquad \text{for } E < E_{\rm c}^{+} \\ \rho_0 T_6^{-1} \qquad \text{for } E > E_{\rm c}^{+} \end{cases} \quad \text{(A10)}$$

$$\rho_{\rm d}^{-}(E) = \begin{cases} \rho_0 T_6^{-1} - (\kappa_{\rm H}/\kappa_{\rm L} - 1)\,(E/\zeta)^2 \\ \qquad \text{for } E < E_{\rm c}^{-} \\ \rho_0 T_6^{-1}\kappa_{\rm L}/\kappa_{\rm H} \qquad \text{for } E > E_{\rm c}^{-} \end{cases} , \quad \text{(A11)}$$

where

$$E_{\rm c}^{+} = \zeta\rho_0^{1/2} T_6^{-1/2} \quad \text{(A12)}$$

$$E_{\rm c}^{-} = \zeta\rho_0^{1/2} T_6^{-1/2}(\kappa_{\rm L}/\kappa_{\rm H})^{1/2}. \quad \text{(A13)}$$

Equations (A10) and (A11), along with the corresponding decoupling depths for the plus and minus-modes, are also plotted in Fig. A18.

A1.3 Numerical Method

Using the opacities of Models (a) and (b) in our magnetic diffusion atmosphere code (for simplicity and computation speed) described in Paper I, we obtain self-consistent atmosphere models for a given choice of ζ, λ, $\kappa_{\rm H}$, and $\kappa_{\rm L}$. The results presented in this section are somewhat modified for a full, angle-dependent solution of the radiative transfer equation, but since here we are more interested in the qualitative effects of vacuum polarization, the diffusion models are adequate for illustrative purposes. Temperature corrections and deviations from radiative equilibrium and constant flux are 1% (see Paper I).

For illustrative purposes, we choose the parameters ζ, λ, $\kappa_{\rm H}$, and $\kappa_{\rm L}$ for the toy models that roughly correspond to the case of an atmosphere with magnetic field $B = 5 \times 10^{14}$ G. For this magnetic field, equations (2.39)-(2.41) give $\zeta \approx B_{14}^{-1} f(B) \approx 0.3$. We choose a fairly broad width $(\lambda - 1) = 0.3$ for the feature so that the required grid resolution is not too computationally demanding. We also choose values for the parameters $\kappa_{\rm H} = \kappa_0^{\rm es}$ and $\kappa_{\rm L} = 10^{-4}\kappa_0^{\rm es}$ so that the equivalent width of the feature $(\kappa_{\rm H}/\kappa_{\rm L})(1-\lambda^{-2}) = 4000$, which corresponds roughly to the equivalent width of the vacuum resonance feature for $B = 5\times10^{14}$ G [see eq. (3.23)].

As discussed in Section 5, to correctly account for the density-dependent opacity feature, such as in Model (a), in numerical calculations, it is important that the density or depth grid is sufficiently dense so that the opacity features at neighboring density grid points overlap. For Model (a) with $\lambda = 1.3$, the minimum required grid spacing is $|\Delta\rho|/\rho < (\lambda-1)^2 = 0.09$. In our calculations, we use 50 grid points per decade in τ (the total number of depth grid points is then $D \approx 350$ covering seven decades in τ), which corresponds to $(\rho_i - \rho_{i-1})/\rho_i \sim 0.04 - 0.05$. In addition, to obtain an accurate representation of the opacity feature in the energy domain, we choose an energy grid that is determined from the depth grid: for each depth grid point, we place an energy grid point on either side of the opacity edge, so that the total number of energy grid points $N = 4D$ for Model (a) and $N = 2D$ for Model (b). In this way, we completely characterize the shape and strength of the opacity features in Models (a) and (b).

A1.4 Numerical Results

Figure A19 plots the temperature profiles for the atmosphere models with $T_{\rm eff} = 5 \times 10^6$ K using Model (a) (mimicking the case of no mode conversion) and Model (b) (mimicking the case of complete mode conversion) and $\zeta = 0.3$, $\lambda = 1.3$, $\kappa_{\rm H} = \kappa_0^{\rm es}$, and $\kappa_{\rm L} = 10^{-4}\kappa_0^{\rm es}$. Also shown is the temperature profile from a double-grey atmosphere, i.e., two photon modes each with constant opacities $\kappa_{\rm E}^{X} = \kappa_{\rm L}$ for the X-mode and $\kappa_{\rm E}^{O} = \kappa_{\rm H}$ for the O-mode. We see that both Model (a) and Model (b) have higher temperatures (at all depths) than the double-grey case. This is due to the heating effect associated with the increase in opacity (see Section 6 and Figs. A7 and A8). Also note the temperature inversions that occur near $\tau \sim 600$; this is due to the absorption of high-energy X-ray photons as they encounter the resonance feature. Figure A20 shows the corresponding spectra of the atmosphere models. Note that all of these spectra are harder than a blackbody at $T = 5 \times 10^6$ K and are similar to the behavior seen in Fig. A11, except without the ion cyclotron line.

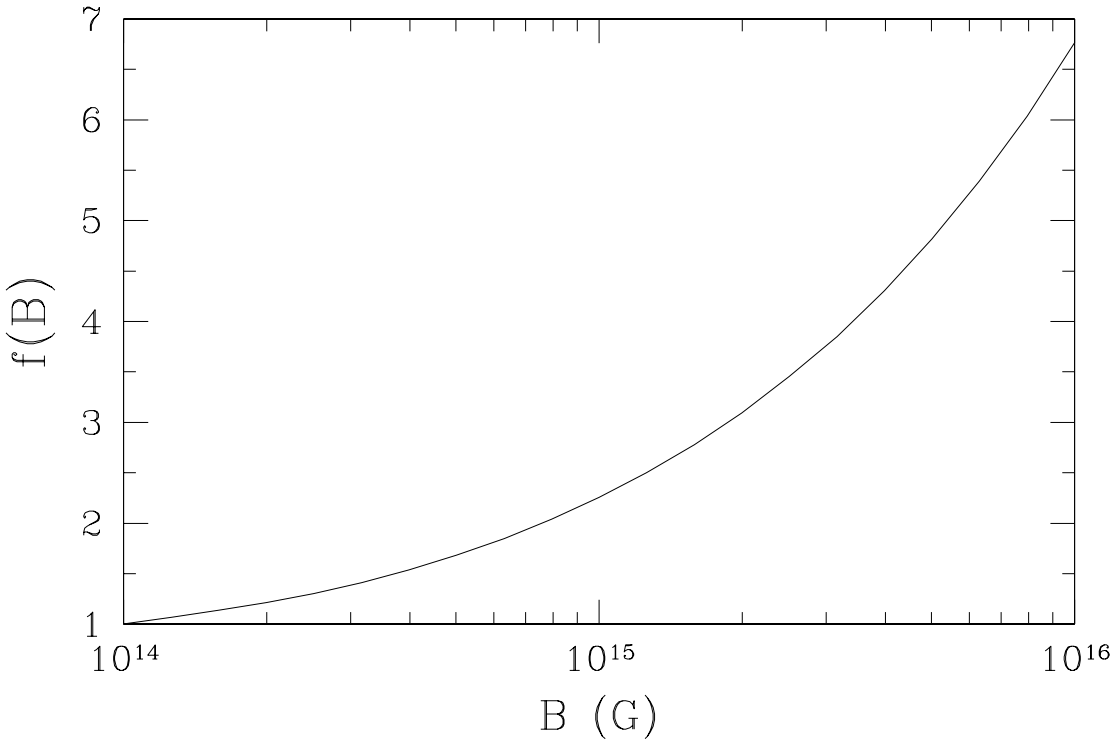

Figure A1. The ratio $f(B) = E_{\rm V}(B)/E_{\rm V}^{(0)}(B)$ as a function of B, where $E_{\rm V}(B)$ is the vacuum resonance energy [eq. (2.38)] and $E_{\rm V}^{(0)}(B) = E_{\rm V}(B \ll B_{\rm Q})$ [eq. (2.39)].

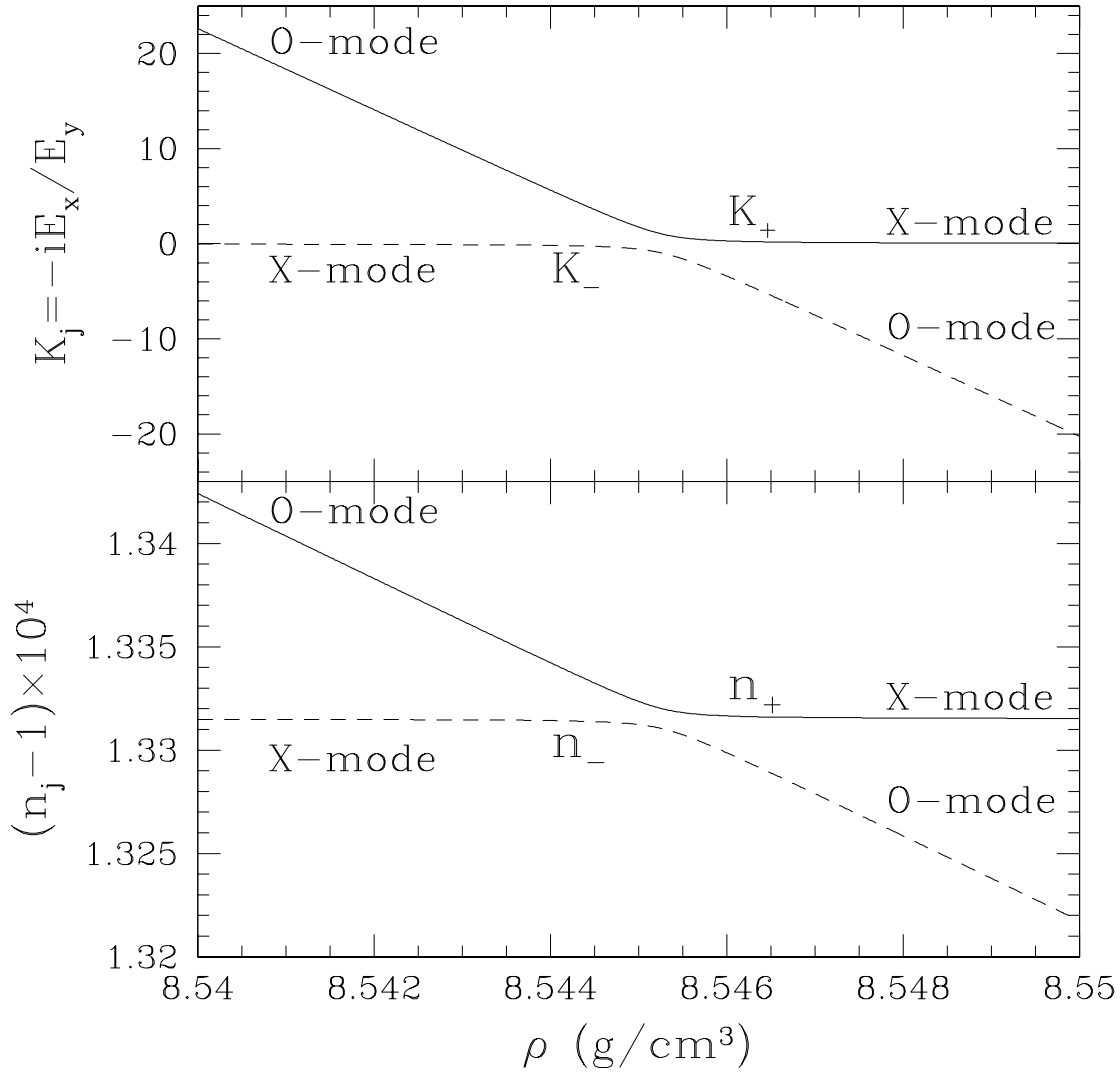

Figure A2. The polarization ellipticities K_j [upper panel; see eq. (2.43)] and refractive indices n_j [lower panel; see eq. (2.34)] of the photon modes as functions of density near the vacuum resonance for $B = 5 \times 10^{14}$ G, $\theta_B = 45°$, $E = 1$ keV, and $Y_e = 1$.

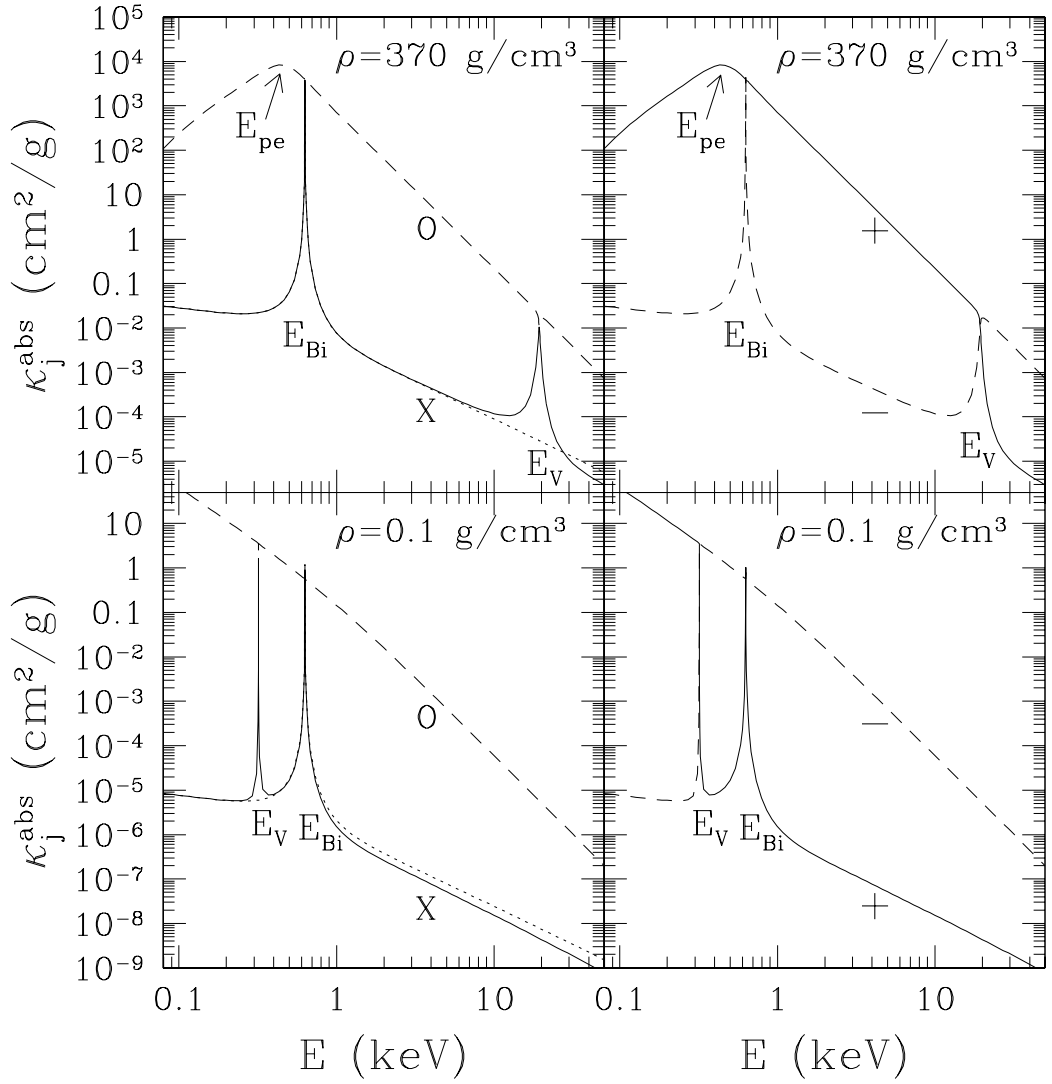

Figure A3. Absorption opacity $\kappa_j^{\rm abs}$ as a function of energy for $B = 10^{14}$ G, $\theta_B = 45°$, and $T = 7 \times 10^6$ K at $\rho = 370\,{\rm g\ cm^{-3}}$ (upper panels) and $\rho = 0.1\,{\rm g\ cm^{-3}}$ (lower panels). The left panels show the opacities for the X-mode ($j = 1$, solid lines) and the O-mode ($j = 2$, dashed lines), while the right panels are for the plus-mode ($j = +$, solid lines) and the minus-mode ($j = -$, dashed lines). In the left panels, the dotted lines show the the X-mode opacity when vacuum polarization is neglected. Several features are marked in the figure: E_{Bi} is the ion cyclotron energy, $E_{\rm V}$ is the vacuum resonance energy, and $E_{\rm pe}$ is the electron plasma energy. The variations of the O-mode opacity at $E \lesssim E_{\rm pe}$ are due to $K_{z,j}$ [$\propto \omega_{\rm pe}^2$; see eq. (2.33)].

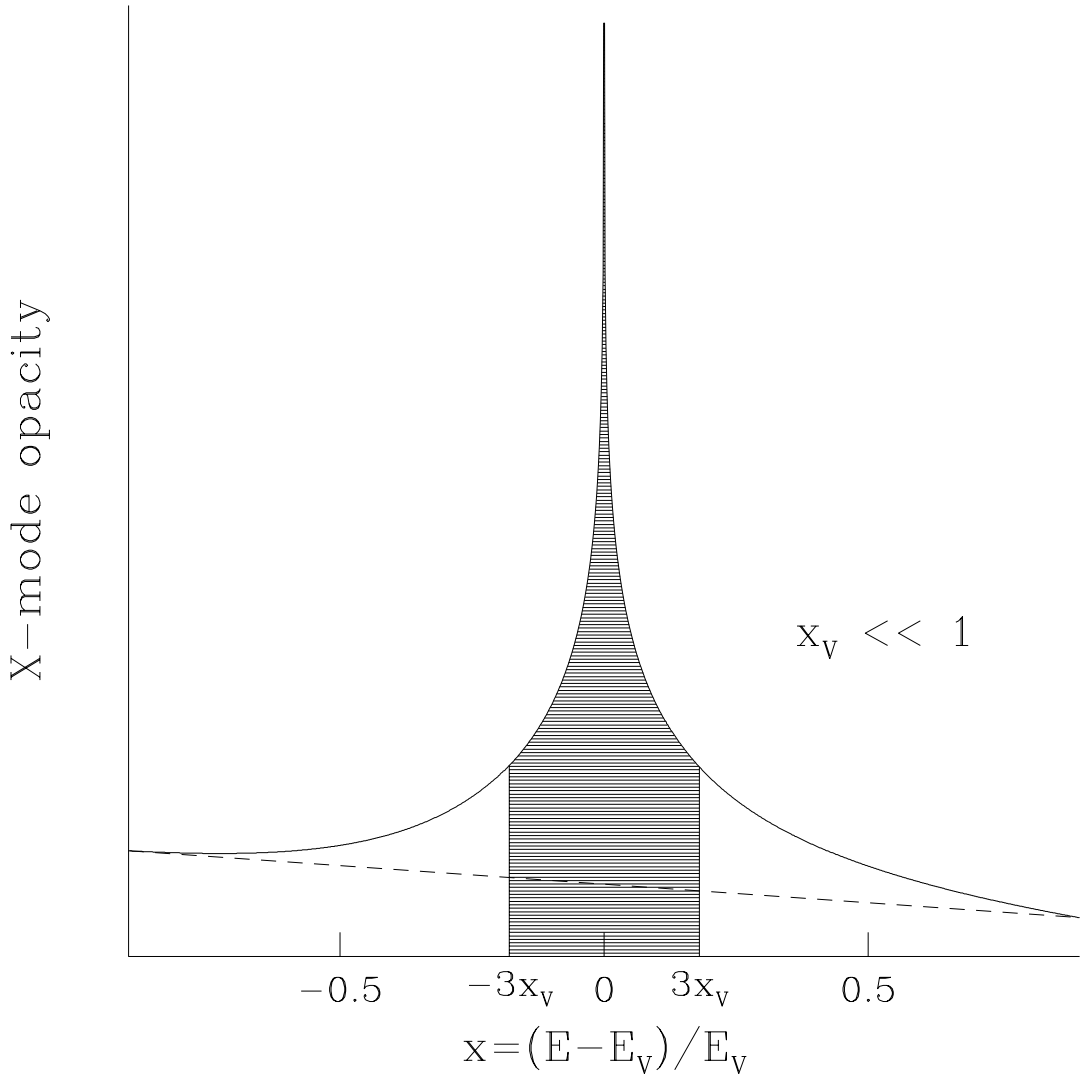

Figure A4. A schematic picture of the X-mode opacity near the vacuum resonance energy $E_{\rm V}$. The dashed line represents the opacity when vacuum polarization is neglected. The shaded region, $-3x_{\rm V} \lesssim x \lesssim 3x_{\rm V}$ [see eq. (3.19); note that $x_{\rm V} \ll 1$], provides the dominant contribution to the equivalent width of the vacuum resonance feature [eqs. (3.22) and (3.23)], although a much broader region, $-0.5 \lesssim x \lesssim 0.5$, is affected by vacuum polarization. The opacity at the resonance ($E = E_{\rm V}$) is $\sim u_{\rm e}$ times larger than the continuum.

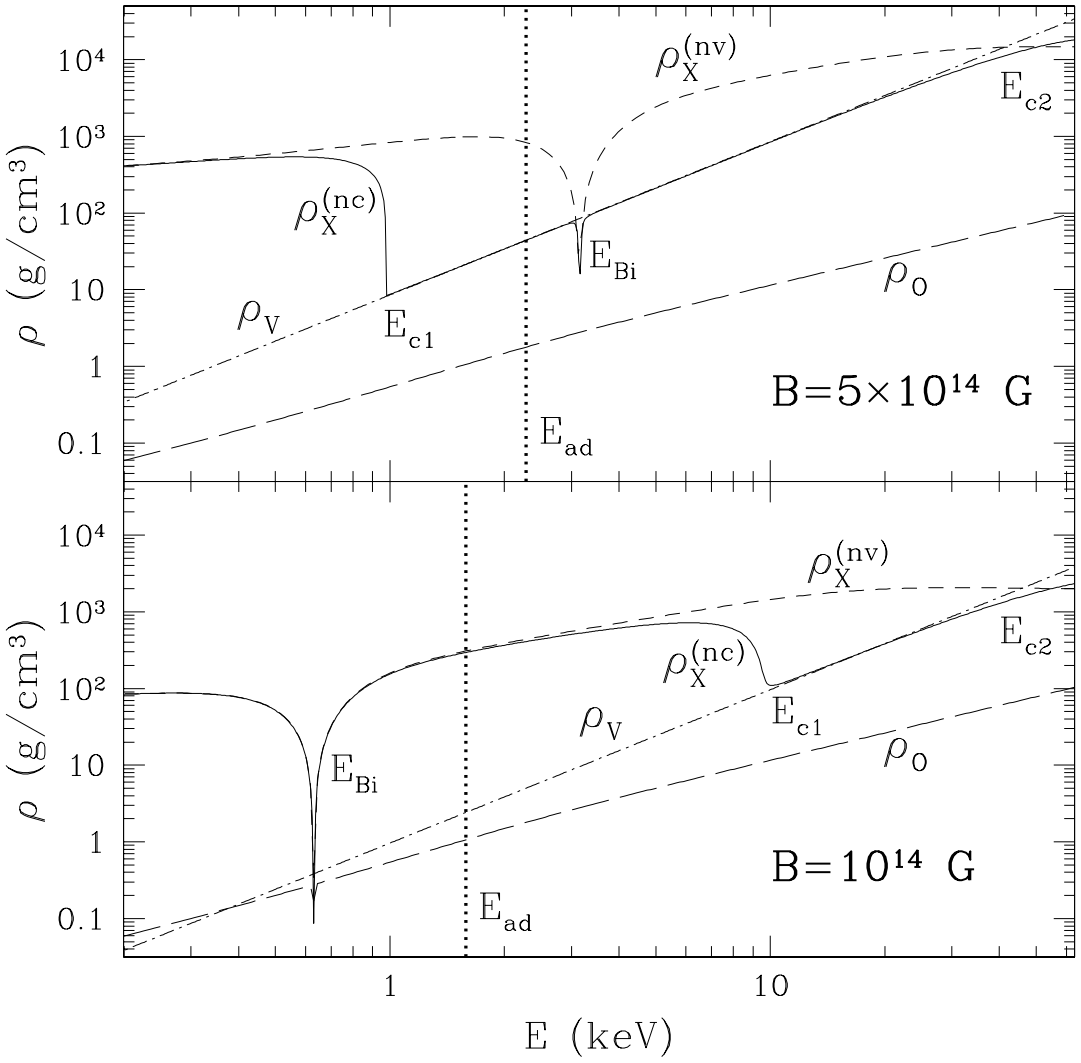

Figure A5. The density at which photons of different polarization modes decouple from the matter as a function of photon energy for $T = 5 \times 10^6$ K, $\theta_B = 45°$, and $B = 10^{14}$ G (lower panel) and $B = 5 \times 10^{14}$ G (upper panel). The solid lines show the X-mode decoupling density $\rho_X^{(\rm nc)}$ when vacuum polarization is included but mode conversion is neglected, the short-dashed lines are for $\rho_X^{(\rm nv)}$ with no vacuum polarization, the long-dashed lines are for the O-mode ρ_O (note that ρ_O is unaffected by the magnetic field and vacuum polarization effects), and the dot-dashed lines show the vacuum resonance density $\rho_{\rm V}$ [eq. (2.42)]. The vertical dotted lines denote the critical energy $E_{\rm ad}$ for adiabatic mode conversion [eq. (2.45)]. In general, vacuum polarization (including the mode conversion effect) reduces the decoupling density of X-mode photons with energies between $\min(E_{\rm c1}, E_{\rm ad})$ and $E_{\rm c2}$, where $E_{\rm c1}$ and $E_{\rm c2}$ are given approximately by equations (4.4) and (4.3), respectively. The ion cyclotron resonance $E_{Bi} = 0.63\, B_{14}$ is clearly evident, though it can be suppressed when vacuum polarization is taken into account, as in the case of $B = 5 \times 10^{14}$ G.

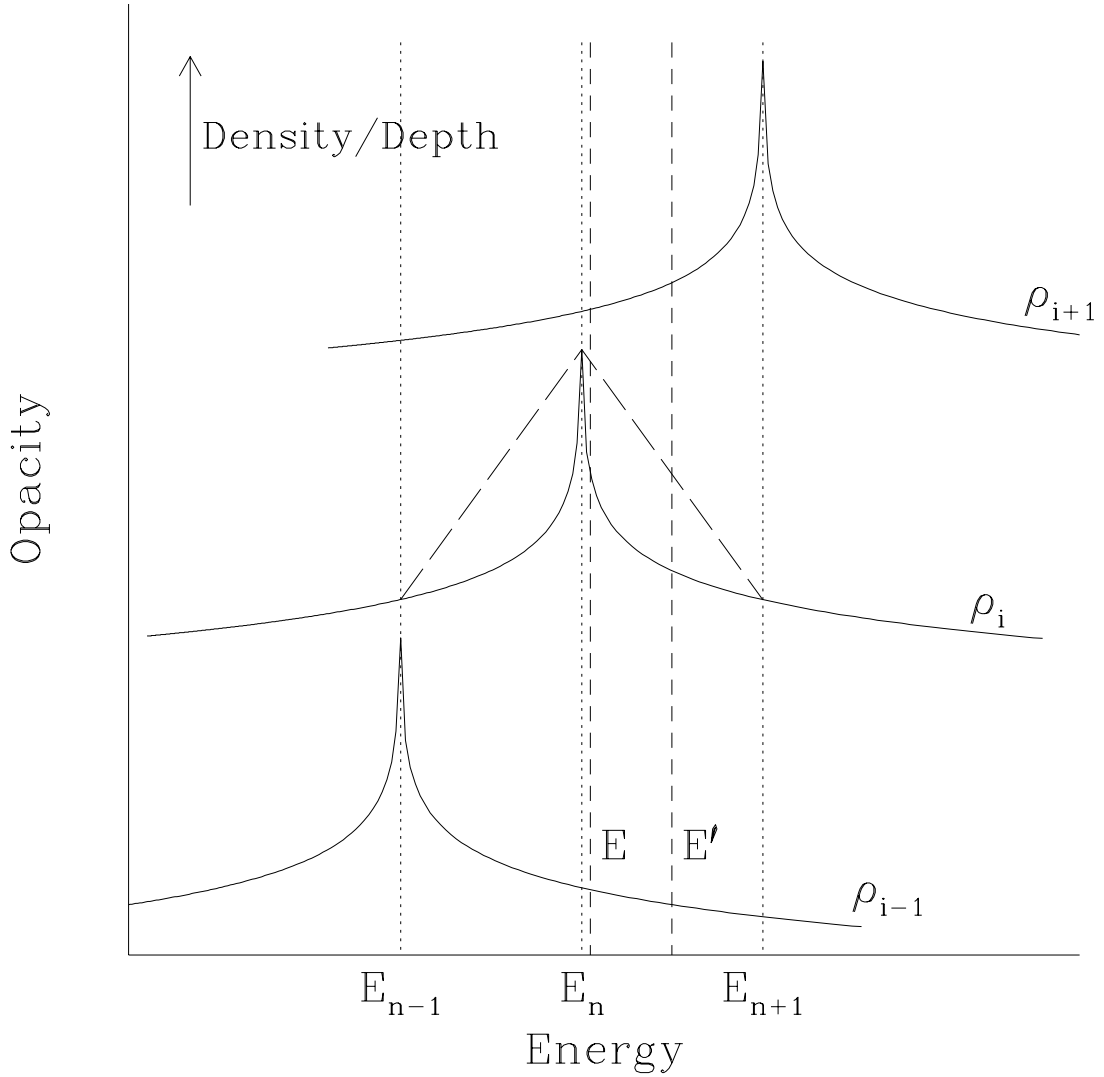

Figure A6. A schematic picture of the radiative opacity as a function of energy at three neighboring density grid points ρ_{i-1}, ρ_i, ρ_{i+1}. Density and depth increase upwards, and the vacuum resonance feature occurs at a higher energy in deeper levels [see eqs. (2.39) or (2.40)]. The opacity at a given depth has been offset for clarity. In the "equal grid" method, the energy grid points E_{n-1}, E_n, E_{n+1} are chosen to be equal to the vacuum resonance energy at one of the density grid points, i.e., $E_n = E_{\rm V}(\rho_i)$. The long-dashed line for ρ_i indicates the apparent opacity obtained by interpolating energy grid points E_{n-1}, E_n, and E_{n+1} (see Section 5.1). The energy E lies close to one of the resonance energies, while E' lies outside any resonance region.

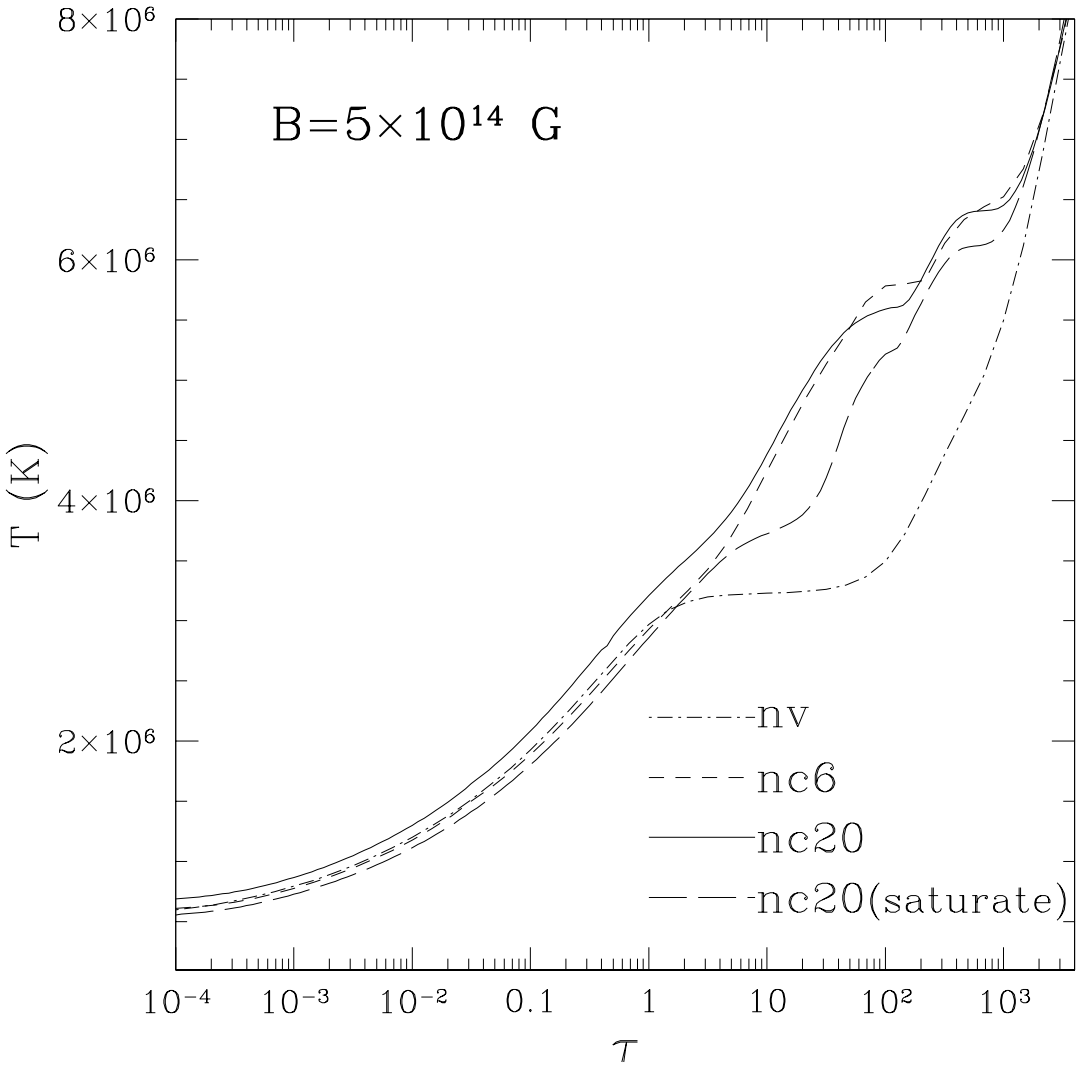

Figure A7. Temperature T as a function of Thomson depth τ for fully ionized hydrogen atmospheres with $B = 5 \times 10^{14}$ G, $\Theta_B = 0$, and $T_{\rm eff} = 5 \times 10^6$ K. The curves marked "nc#" are models which include vacuum polarization but no mode conversion using the "equal grid" method described in Section 5.1, with "#" indicating the number of grid points per decade in τ. The long-dashed line is for the same model as "nc20" but restricting $\beta_{\rm V} \geq 10^{-2}$ (see Section 6.3), while the dot-dashed line is for the model with no vacuum polarization (nv).

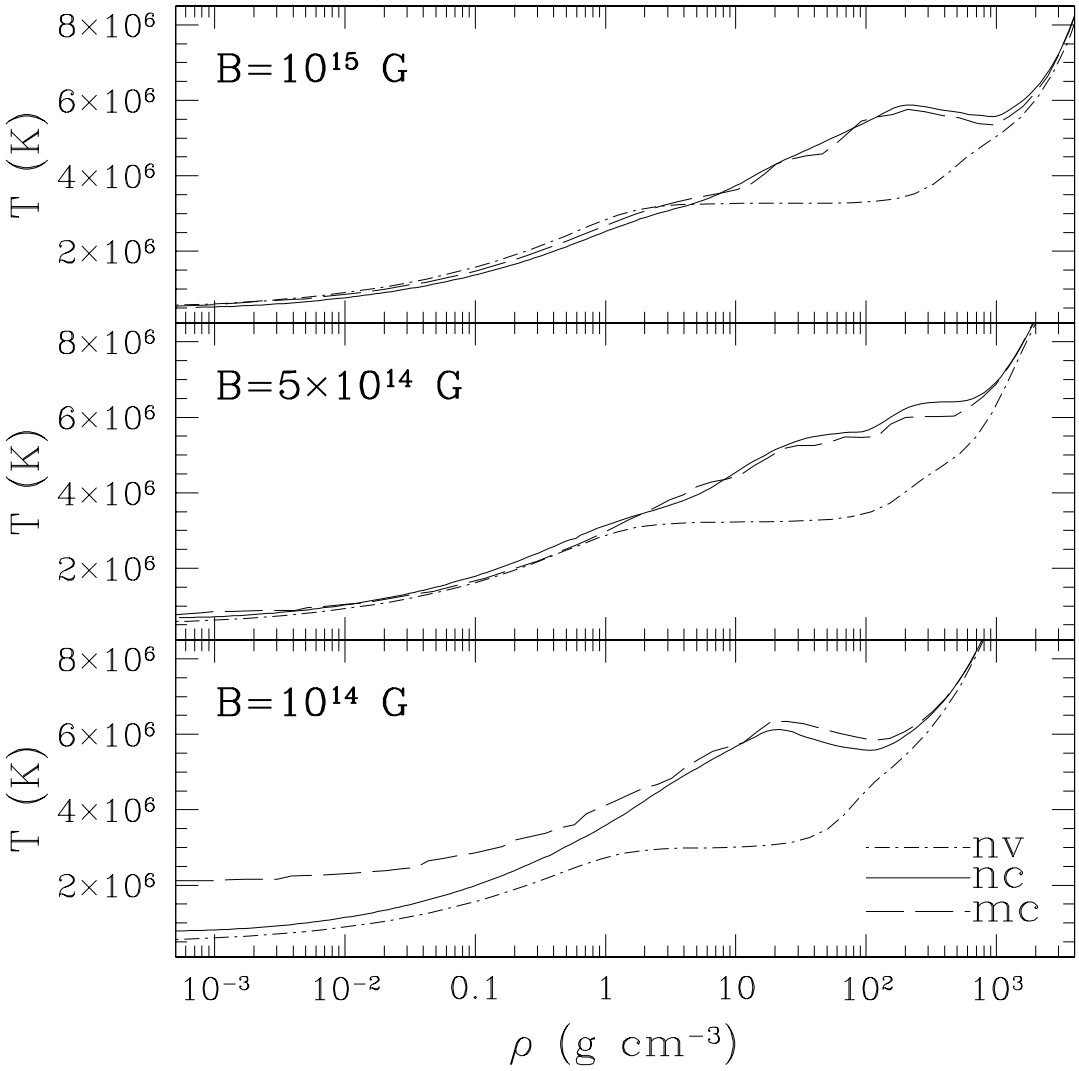

Figure A8. Temperature T as a function of density ρ for fully ionized hydrogen atmospheres with $T_{\rm eff} = 5 \times 10^6$ K, $\Theta_B = 0$, and $B = 10^{14}$ G (lower panel), $B = 5 \times 10^{14}$ G (middle panel), $B = 10^{15}$ G (upper panel). The solid lines are for models with vacuum polarization but no mode conversion (nc), the dashed lines are for models which assume complete mode conversion (mc), and the dot-dashed lines are for models with no vacuum polarization (nv).

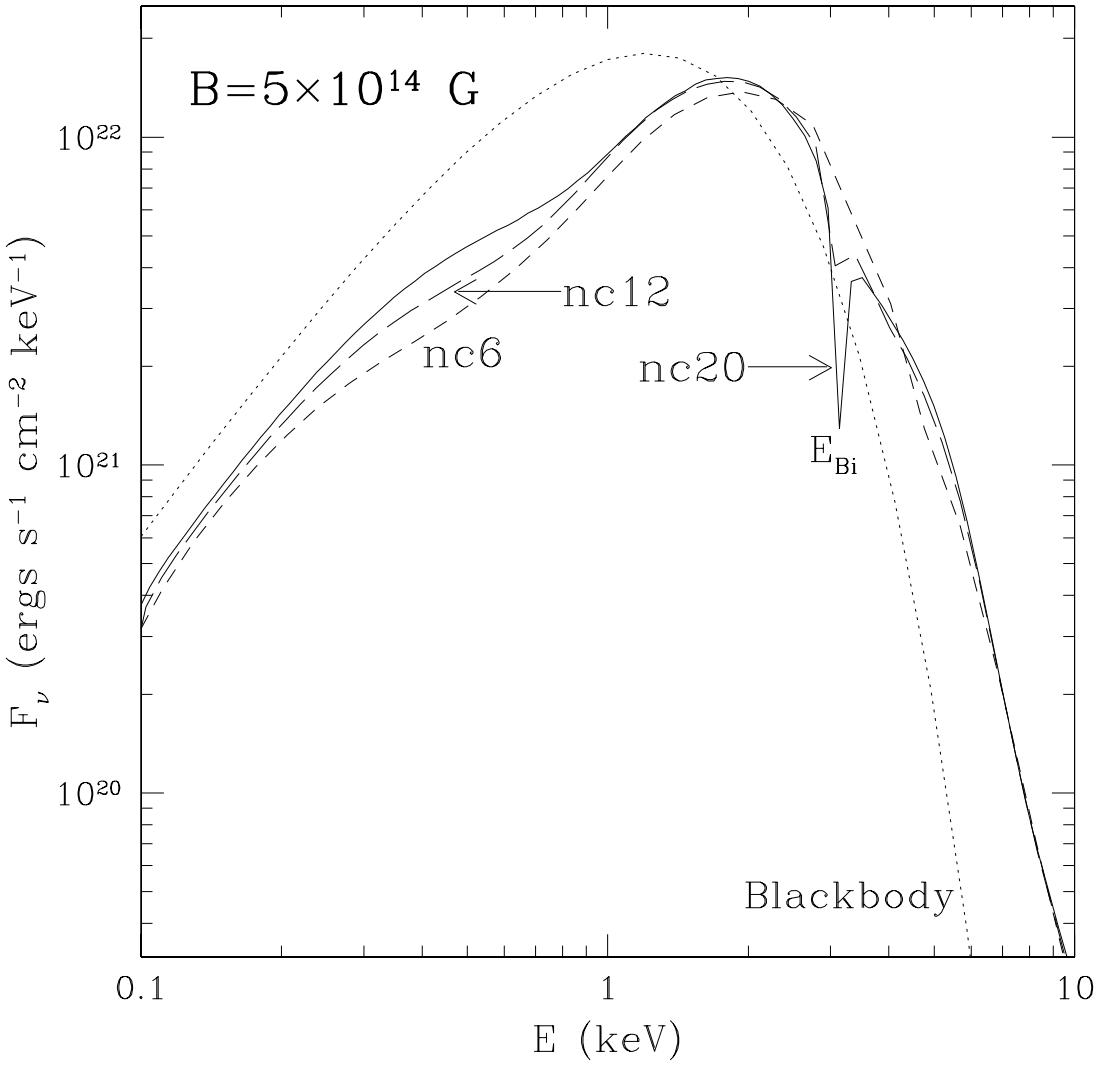

Figure A9. Spectra of fully ionized hydrogen atmospheres with $B = 5 \times 10^{14}$ G, $\Theta_B = 0$, and $T_{\rm eff} = 5 \times 10^6$ K. The curves marked "nc#" are models which include vacuum polarization but no mode conversion using the "equal grid" method described in Section 5.1, with "#" indicating the number of grid points per decade in τ. The corresponding temperature profiles are shown in Fig. A7. The dotted line is for a blackbody with $T = 5 \times 10^6$ K. Note that the absence of the ion cyclotron feature at E_{Bi} for model nc6 is an artifact of the low grid resolution.

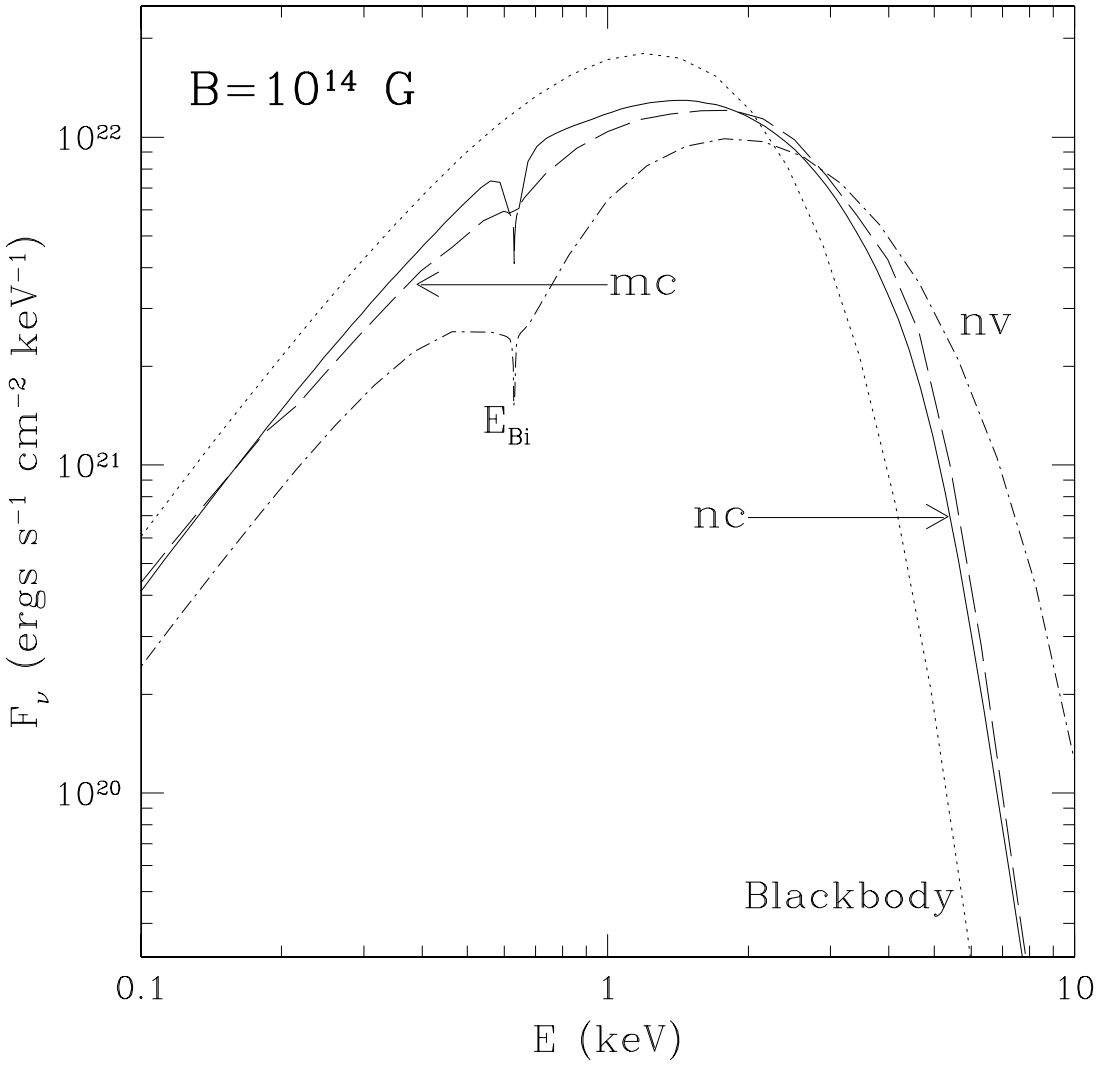

Figure A10. Spectra of fully ionized hydrogen atmospheres with $B = 10^{14}$ G, $\Theta_B = 0$, and $T_{\rm eff} = 5 \times 10^6$ K. The solid line is for an atmosphere with vacuum polarization but no mode conversion (nc), the dashed line is for an atmosphere with complete mode conversion (mc), the dot-dashed line is for an atmosphere with no vacuum polarization (nv), and the dotted line is for a blackbody with $T = 5 \times 10^6$ K. The $E_{Bi} = 0.63$ keV ion cyclotron feature (from ~ 0.4 to ~ 1 keV) has an equivalent width ~ 140 eV when vacuum polarization is not included (model nv) but is only ~ 20 eV in the no mode conversion case (model nc) and ~ 8 eV in the complete mode conversion case (model mc).

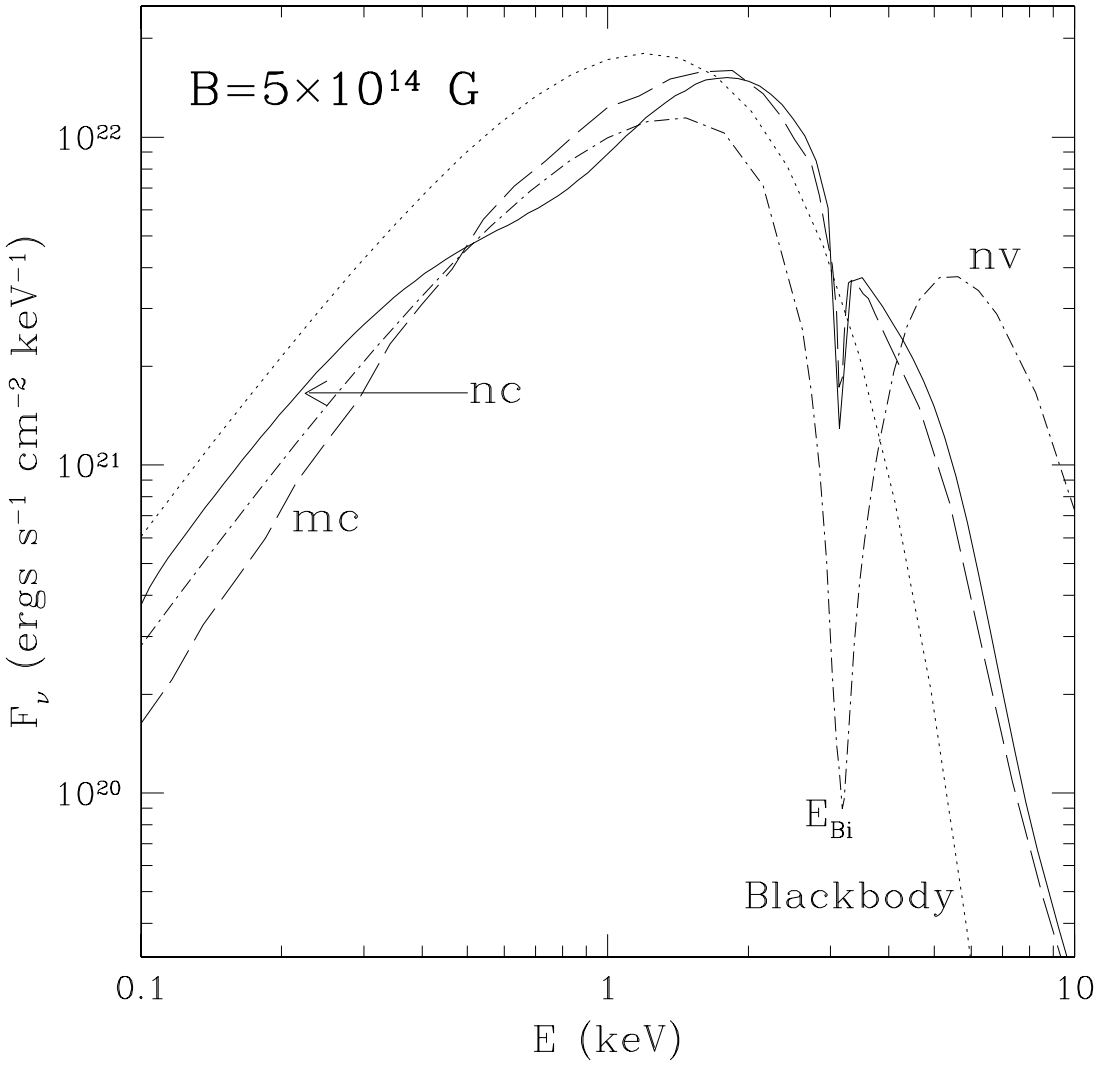

Figure A11. Spectra of fully ionized hydrogen atmospheres with $B = 5 \times 10^{14}$ G, $\Theta_B = 0$, and $T_{\rm eff} = 5 \times 10^6$ K. The solid line is for an atmosphere with vacuum polarization but no mode conversion (nc), the dashed line is for an atmosphere with complete mode conversion (mc), the dot-dashed line is for an atmosphere with no vacuum polarization (nv), and the dotted line is for a blackbody with $T = 5 \times 10^6$ K. The $E_{Bi} = 3.15$ keV ion cyclotron feature (from ~ 2 to ~ 5 keV) has an equivalent width ~ 2 keV when vacuum polarization is not included (model nv) but is only ~ 0.1 keV in the no mode conversion case (model nc) and ~ 0.09 keV in the complete mode conversion case (model mc).

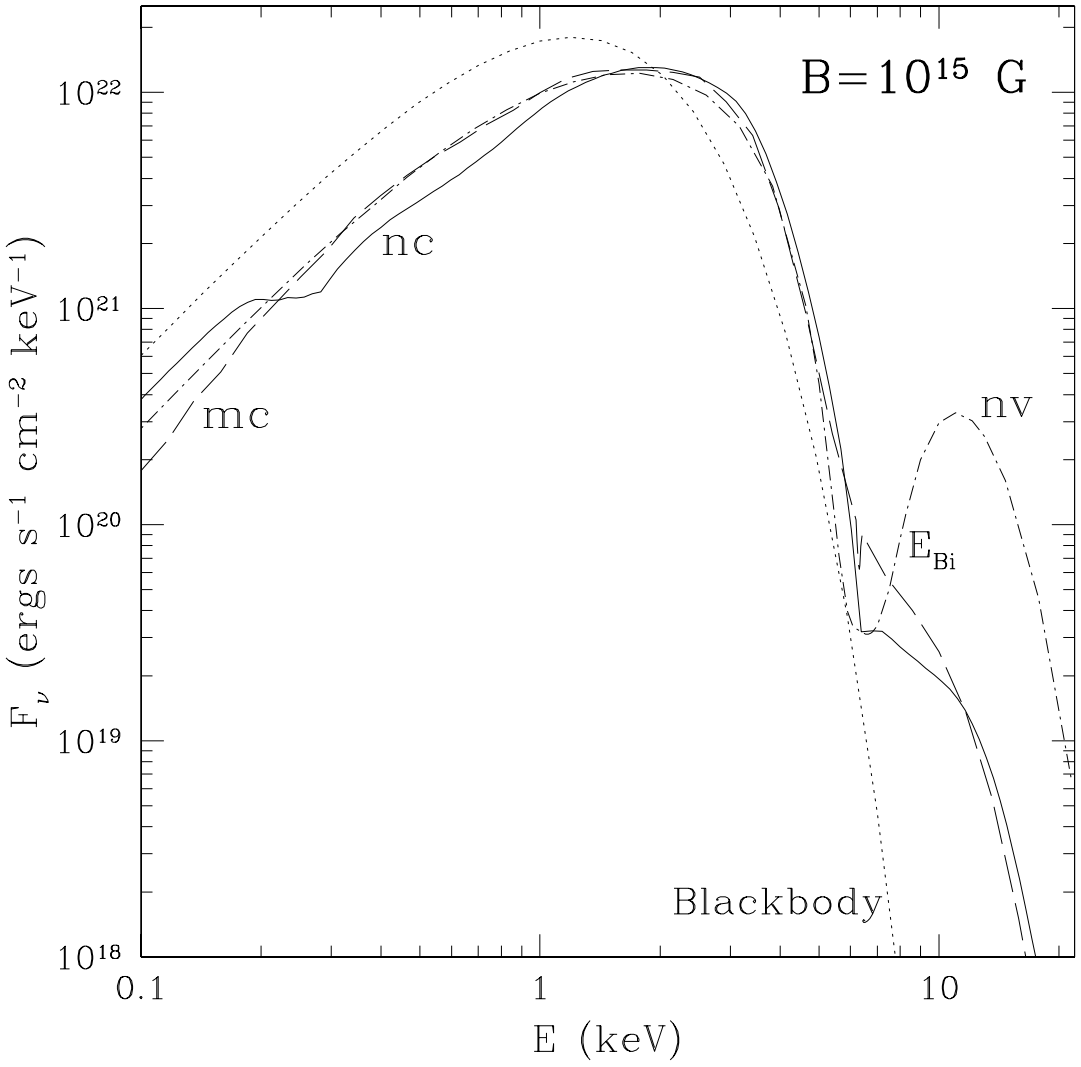

Figure A12. Spectra of fully ionized hydrogen atmospheres with $B = 10^{15}$ G, $\Theta_B = 0$, and $T_{\rm eff} = 5 \times 10^6$ K. The solid line is for an atmosphere with vacuum polarization but no mode conversion (nc), the dashed line is for an atmosphere with complete mode conversion (mc), the dot-dashed line is for an atmosphere with no vacuum polarization (nv), and the dotted line is for a blackbody with $T = 5 \times 10^6$ K. The $E_{Bi} = 6.3$ keV ion cyclotron feature (from ~ 5 to ~ 10 keV) has an equivalent width ~ 4 keV when vacuum polarization is not included (model nv) but is only ~ 0.2 keV in the no mode conversion case (model nc) and ~ 0.05 keV in the complete mode conversion case (model mc).

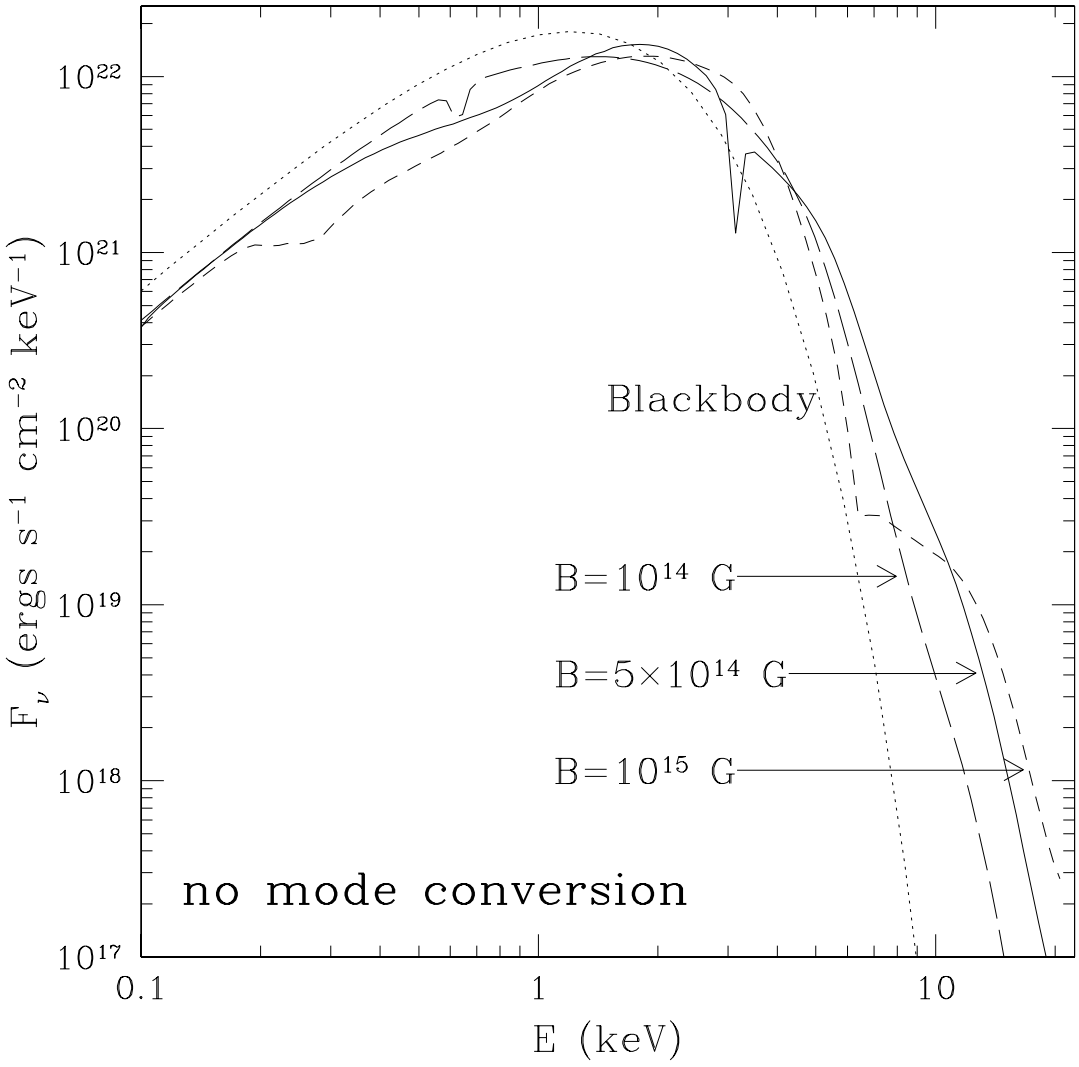

Figure A13. Spectra of fully ionized hydrogen atmospheres with $\Theta_B = 0$ and $T_{\rm eff} = 5 \times 10^6$ K when vacuum polarization is included but mode conversion is neglected (nc). The long-dashed line is for the $B = 10^{14}$ G atmosphere, the solid line is for the $B = 5 \times 10^{14}$ G atmosphere, the short-dashed line is for the $B = 10^{15}$ G atmosphere, and the dotted line is for a blackbody with $T = 5 \times 10^6$ K.

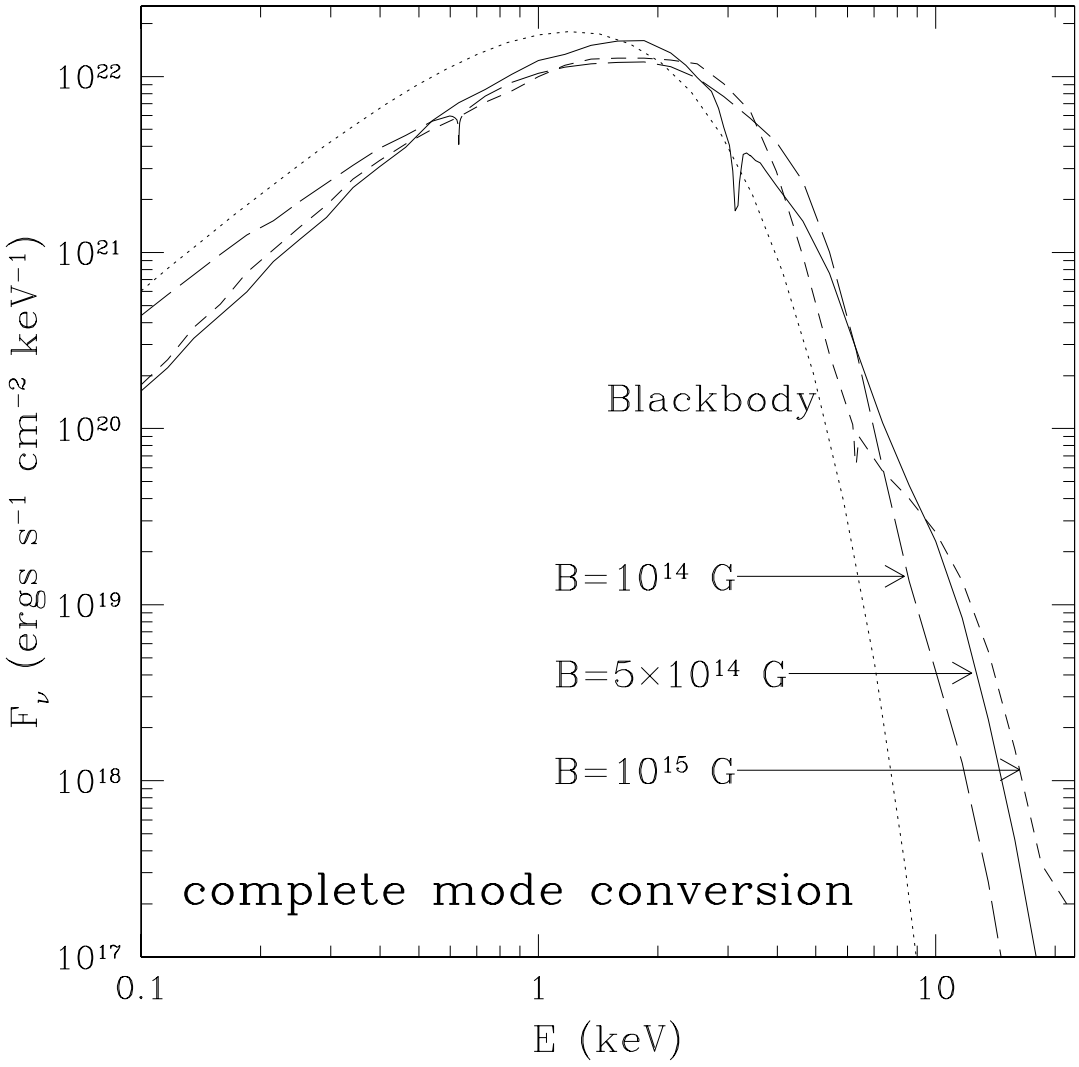

Figure A14. Spectra of fully ionized hydrogen atmospheres with $\Theta_B = 0$ and $T_{\rm eff} = 5 \times 10^6$ K when mode conversion is complete (mc). The long-dashed line is for the $B = 10^{14}$ G atmosphere, the solid line is for the $B = 5 \times 10^{14}$ G atmosphere, the short-dashed line is for the $B = 10^{15}$ G atmosphere, and the dotted line is for a blackbody with $T = 5 \times 10^6$ K.

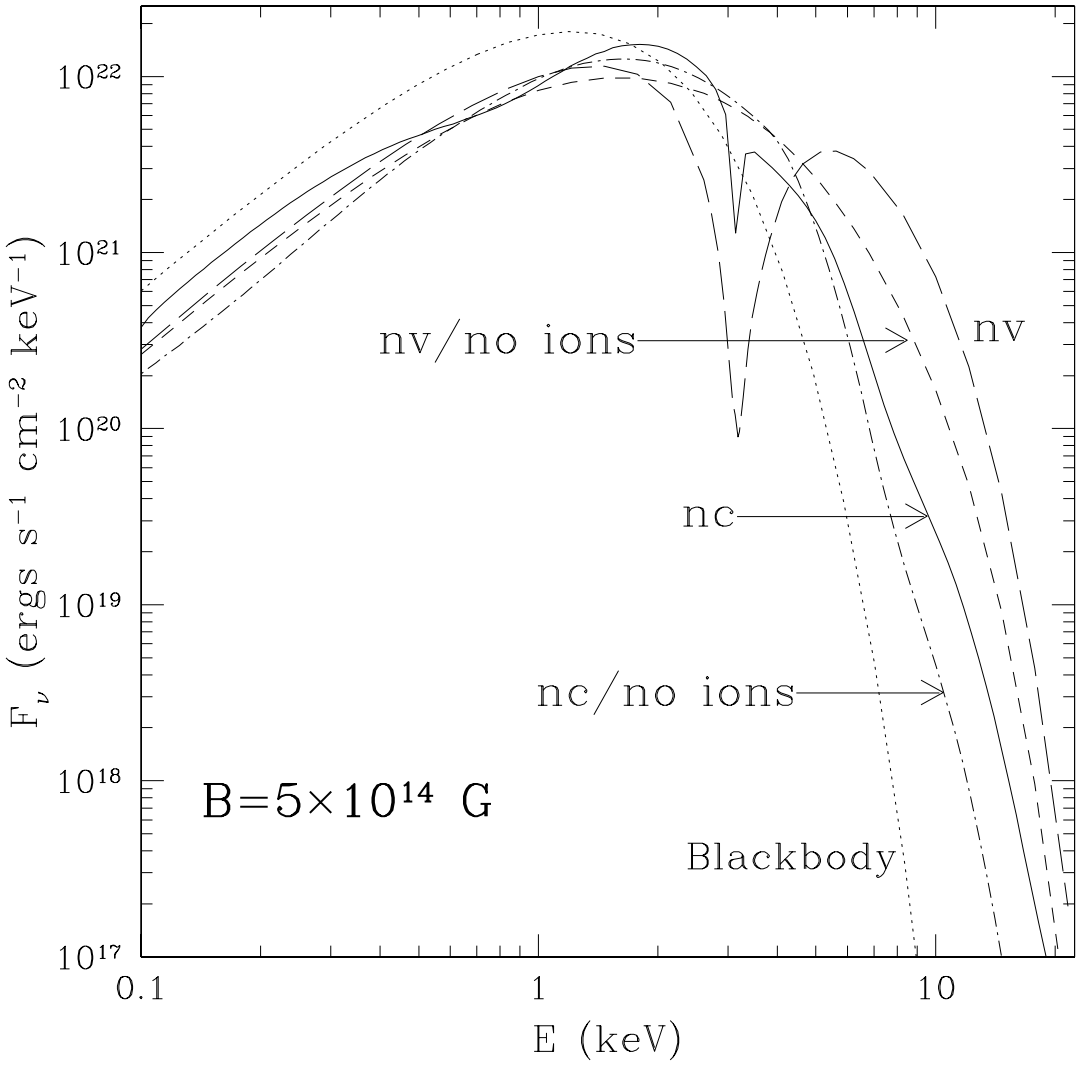

Figure A15. Spectra of fully ionized hydrogen atmospheres with $B = 5 \times 10^{14}$ G, $\Theta_B = 0$, and $T_{\rm eff} = 5 \times 10^6$ K. The solid line is for an atmosphere with vacuum polarization but no mode conversion (model nc, which includes ions), the dot-dashed line is for an atmosphere with vacuum polarization but no mode conversion and neglecting ion effects (nc/no ions), the long-dashed line is for an atmosphere with no vacuum polarization (model nv, which includes ions), the short-dashed line is for an atmosphere with no vacuum polarization and neglecting ion effects (nv/no ions), and the dotted line is for a blackbody with $T = 5 \times 10^6$ K.

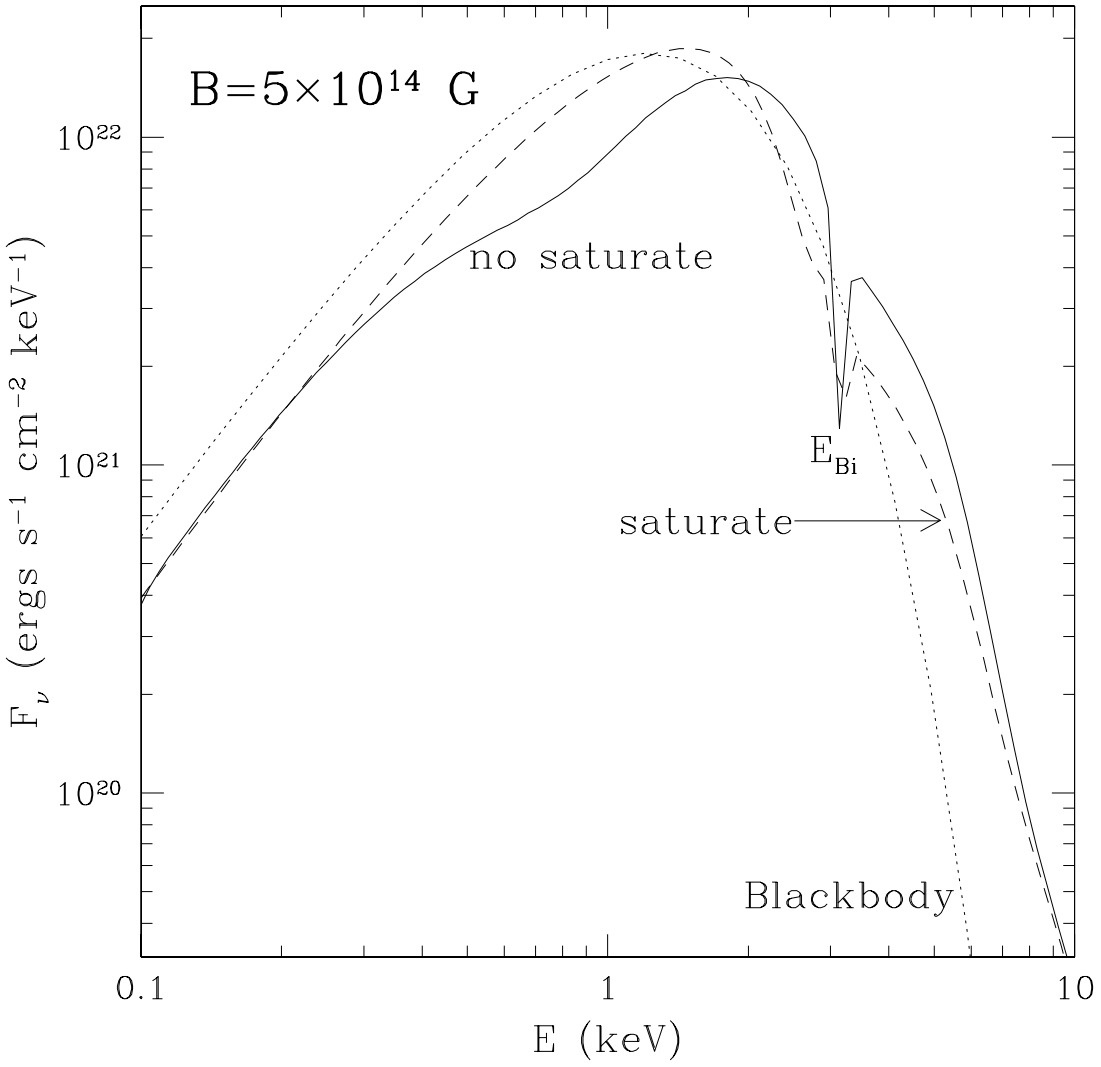

Figure A16. Spectra of fully ionized hydrogen atmospheres with $B = 10^{14}$ G, $\Theta_B = 0$, and $T_{\rm eff} = 5 \times 10^6$ K. The solid line (no saturate) is for an atmosphere with vacuum polarization but no mode conversion using the "equal grid" method described in Section 5.1, the dashed line (saturate) is for the same atmosphere with vacuum polarization but no mode conversion using the "saturation" method described in Section 6.3, and the dotted line is for a blackbody with $T = 5 \times 10^6$ K.

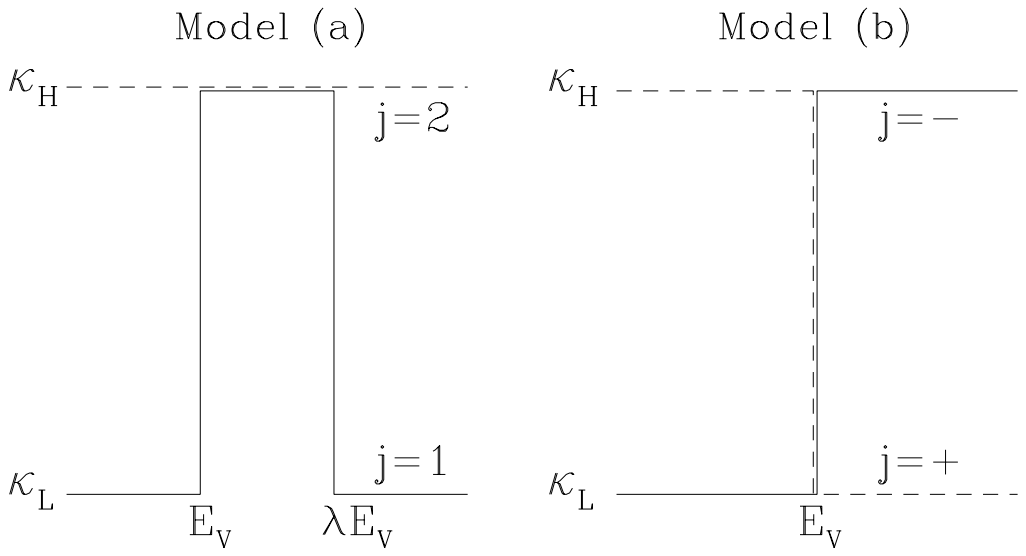

Figure A17. Toy model opacities used in Appendix A1 with $j = 1, 2$ indicating the X and O-mode, respectively, and $j = \pm$ indicating the plus and minus-modes, respectively. Model (a) mimics the case where mode conversion is neglected [see eq. (A1)]; Model (b) mimics the case where mode conversion is complete [see eq. (A3)]. The opacities are parameterized by the location of the resonance feature E_V [eq.(A2)], the width parameter λ, and κ_H and κ_L.

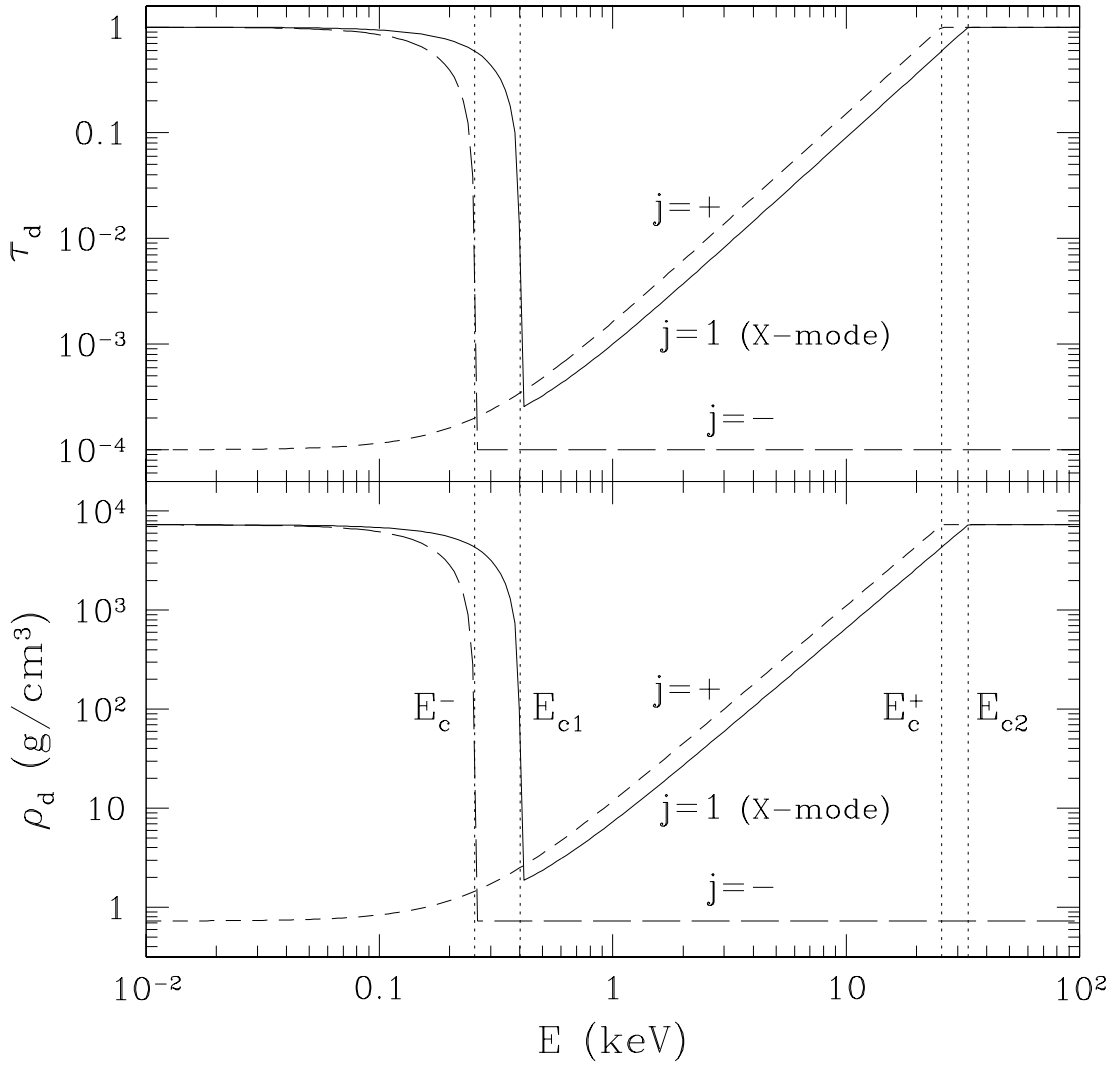

Figure A18. The upper panel shows the optical depth $\tau_{\rm d}$ (in terms of the opacity $\kappa_{\rm L}$) at which photons of different modes decouple from the matter as a function of energy for $T = 5 \times 10^6$ K, $\zeta = 0.3$, $\lambda = 1.3$, $\kappa_{\rm H} = \kappa_0^{\rm es}$, and $\kappa_{\rm L} = 10^{-4}\kappa_0^{\rm es}$. The lower panel shows the corresponding density $\rho_{\rm d}$ at these depths. The solid lines are for the X-mode with an opacity given by Model (a) (the O-mode decoupling depth $\tau_{\rm d} = 1$ is not shown), and the short and long-dashed lines are for Model (b) (see Fig. A17). The vertical dotted lines indicate the critical energies $E_{\rm c1}$ [eq. (A5)], $E_{\rm c2}$ [eq. (A6)], $E_{\rm c}^+$ [eq. (A12)], and $E_{\rm c}^-$ [eq. (A13)].

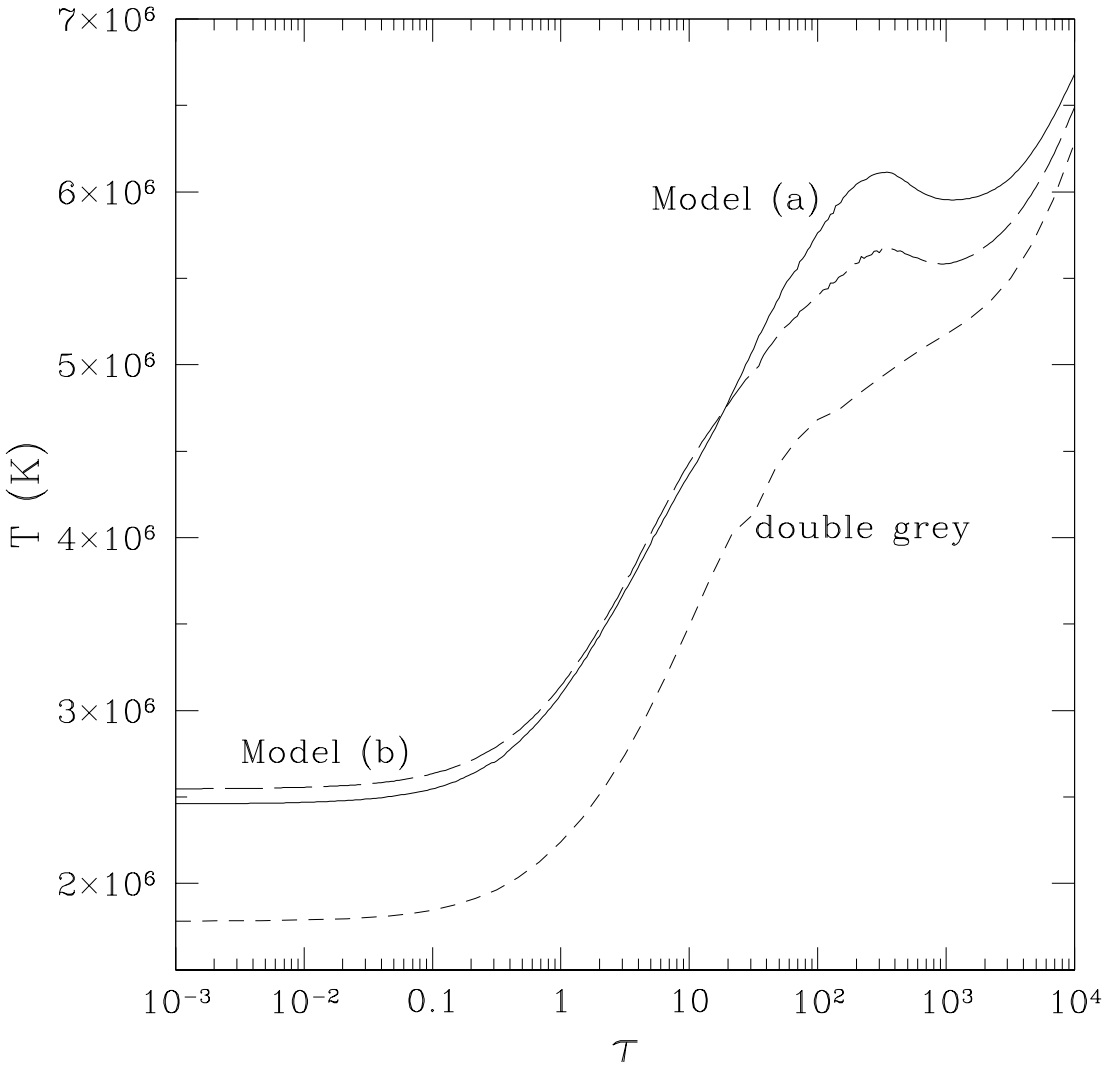

Figure A19. Temperature T as a function of Thomson depth τ for atmosphere models using the toy opacities given in Appendix A1 (see Fig. A17) and $T_{\rm eff} = 5 \times 10^6$ K, $\zeta = 0.3$, $\lambda = 1.3$, $\kappa_{\rm H} = \kappa_0^{\rm es}$, and $\kappa_{\rm L} = 10^{-4}\kappa_0^{\rm es}$. The solid line is for the temperature profile of an atmosphere with Model (a), the long-dashed line is the profile for Model (b), and the short-dashed line is for a double grey atmosphere.

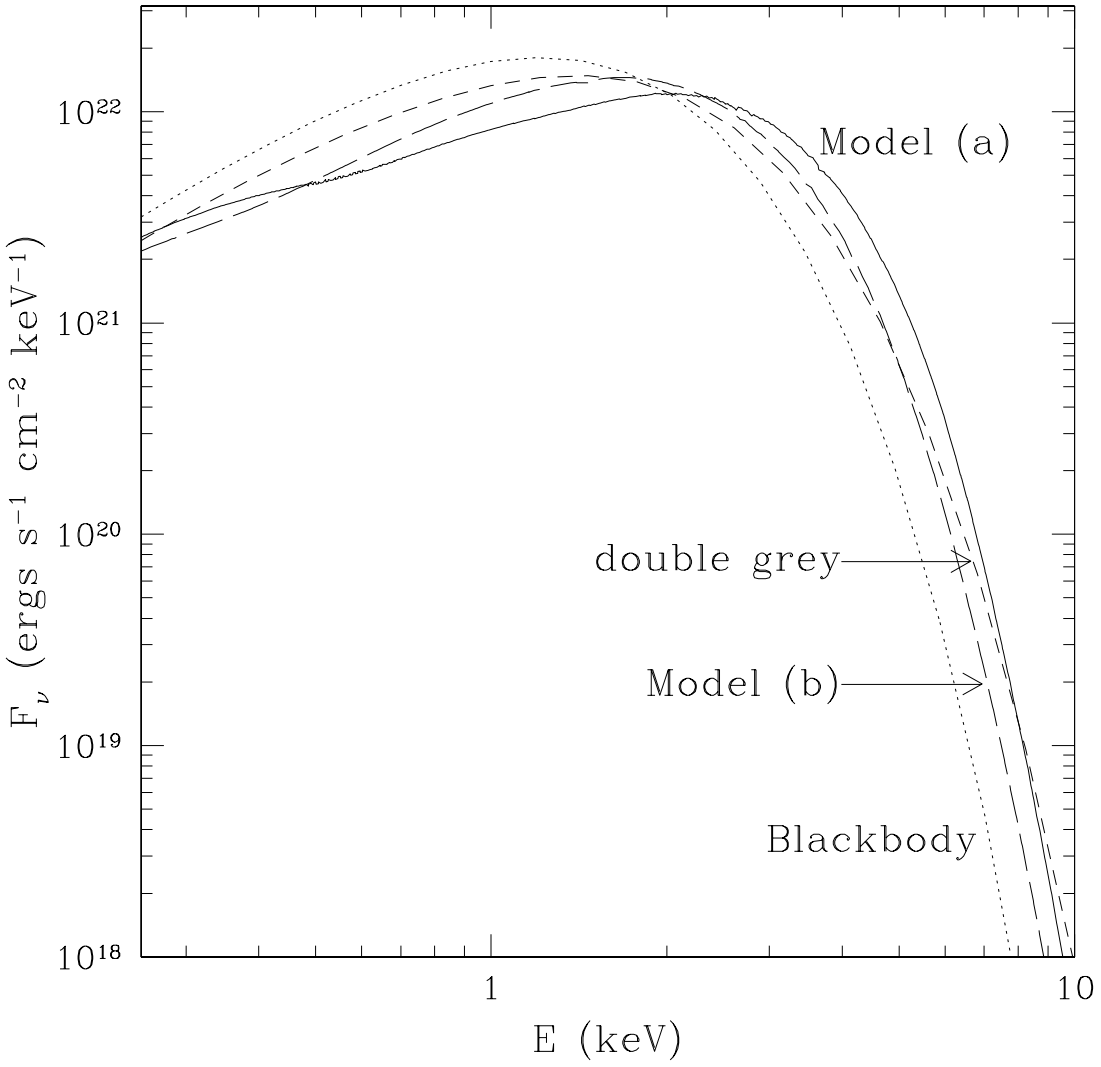

Figure A20. Spectra of atmospheres with $T_{\rm eff} = 5 \times 10^6$ K, $\zeta = 0.3$, $\lambda = 1.3$, $\kappa_{\rm H} = \kappa_0^{\rm es}$, and $\kappa_{\rm L} = 10^{-4}\kappa_0^{\rm es}$. The solid line is for an atmosphere using the Model (a) opacities, the long-dashed line for an atmosphere using the Model (b) opacities, the short-dashed line is for a double grey atmosphere, and the dotted line is for a blackbody with $T = 5 \times 10^6$ K.